DEVELOPMENT OF FUNCTIONAL MULTILAYER COATINGS FOR GAS SENSING AND SMART WINDOW APPLICATIONS

by

CEREN MİTMİT

Submitted to the Graduate School of Engineering and Natural Sciences
in partial fulfillment of the requirements for the degree of
Master of Science

Sabancı University

July 2022

DEVELOPMENT OF FUNCTIONAL MULTILAYER COATINGS FOR GAS SENSING AND SMART WINDOW APPLICATIONS

APPROVED BY:

DATE OF APPROVAL:

ABSTRACT

DEVELOPMENT OF FUNCTIONAL MULTILAYER COATINGS FOR GAS SENSING AND SMART WINDOW APPLICATIONS

CEREN MİTMİT

Materials Science and Nano Engineering, M.Sc. Thesis, July 2022

Thesis Advisor: Asst. Prof. Dr. Eric Meng Meng Tan

Keywords: Multilayer coatings, bandpass filter, infrared, gas detection, smart window, visible light modulation

Functional coatings are used in many areas, from aircraft to optoelectronic devices, energy-saving applications, and sensors. This thesis focuses on designing and developing two functional multilayer coatings. Firstly is the development of a bandpass filter which we combine with a custom-made lithium tantalate pyroelectric detector in an infrared gas detection setup to detect and determine the concentration of ethanol vapor. The constructed bandpass filter that consists of 7-layers of alternating germanium and aluminum oxide materials has a center wavelength of 3250 ± 232 nm and a peak transmittance of 84.5%. This wavelength range overlaps with the characteristic absorption mode of ethanol molecules. In the presence of ethanol vapor in the measuring setup, the pyroelectric detector induces a voltage signal change, thus demonstrating the pyroelectric effect. The measurement system can electronically detect and quantify various concentrations of alcohol (6% - 100% by volume), including alcoholic beverages like beer and wine. The second study focuses on developing a smart window that modulates visible light while reflecting broadband infrared light (2000 – 25000nm). The window is made by placing a thermoresponsive layer between a transparent heater and plexiglass. On a hot day, the thermoresponsive layer (Poly(N-isopropylacrylamide)) can change from the transparent state to the opaque state at its lower critical solution temperature (32.5 °C). Hence, blocking the heat from entering the indoor space. At night, as the temperature drops, the window's opacity can be activated on-demand by activating the transparent heater made from thin layers of aluminum oxide and silver. Therefore, providing users with privacy protection. The window can also reflect a broad spectrum in the infrared, which is well suited for use during cold days. These multiple functionalities of the smart window provide possible solutions to the problems of space heating and cooling that contribute to the high electricity consumption globally.

ÖZET

ÇOK KATMANLI FONKSİYONEL KAPLAMALARIN GAZ ALGILAMA VE AKILLI CAM UYGULAMALARI ÜZERİNE GELİŞTİRİLMESİ

CEREN MİTMİT

Malzeme Bilimi ve Nano Mühendislik, Yüksek Lisans Tezi, Temmuz 2022

Tez Danışmanı: Dr. Öğretim Üyesi Eric Meng Meng Tan

Anahtar kelimeler: Çok katmanlı kaplamalar, bant geçiren filtre, kızılötesi, gaz algılama, akıllı pencere, görünür ışık modülasyonu

Fonksiyonel kaplamalar uçaklardan optoelektronik cihazlara, enerji tasarrufu sağlayan uygulamalardan sensörlere kadar birçok alanda kullanılmaktadır. Bu tez, iki fonksiyonel çok katmanlı kaplama tasarlamaya ve geliştirmeye odaklanmaktadır. Birincisi, etanol buharının konsantrasyonunu tespit etmek ve belirlemek için kızılötesi gaz algılama düzeneğinde özel yapım lityum tantalit piroelektrik dedektörü ile birleştirdiğimiz bir bant geçiren filtrenin geliştirilmesidir. 7 katman alternatif germanyum ve alüminyum oksit malzemeden oluşan yapılandırılmış bant geçiren filtre, 3250 ± 232 nm'lik bir merkez dalga boyuna ve %84,5'lik bir tepe geçirgenliğine sahiptir. Bu dalga boyu aralığı, etanol moleküllerinin karakteristik absorpsiyon modu ile örtüşür. Ölçüm düzeneğinde etanol buharının varlığında, piroelektrik dedektör bir voltaj sinyali değişikliğine neden olur ve böylece piroelektrik etkiyi gösterir. Ölçüm sistemi, bira ve şarap gibi alkollü içecekler dahil olmak üzere çeşitli alkol konsantrasyonlarını (hacimce %6 - %100) elektronik olarak algılayabilir ve ölçebilir. İkinci çalışma, geniş bant kızılötesi ışığı (2000-25000nm) yansıtırken görünür ışığı modüle eden bir akıllı pencere geliştirmeye odaklanıyor. Akıllı pencere, şeffaf bir ısıtıcı ve pleksi arasına ısıya duyarlı bir katman oluşturularak yapıldı. Sıcak bir günde, ısıya duyarlı katman (Poli(N-izopropilakrilamid)), düşük kritik çözelti sıcaklığında (32.5 °C) şeffaf halden opak hale geçebilir. Bu nedenle, ısının iç mekana girmesini engeller. Geceleri, sıcaklık düştükçe, ince alüminyum oksit ve gümüş katmanlarından yapılmış şeffaf ısıtıcıyı etkinleştirerek pencerenin opaklığı isteğe bağlı olarak etkinleştirilebilir. Bu nedenle, kullanıcılara gizlilik koruması sağlar. Pencere ayrıca, soğuk günlerde kullanım için uygun olan kızılötesinde geniş bir spektrumu yansıtabilir. Akıllı pencerenin bu çoklu işlevleri, küresel olarak yüksek elektrik tüketimine katkıda bulunan alan ısıtma ve soğutma sorunlarına olası çözümler sunar.

To my dearest family..

ACKNOWLEDGEMENTS

First and foremost, I am deeply grateful to my supervisor Assist. Prof. Eric Meng Meng Tan for his invaluable supervision, unwavering support and belief in me. What makes me today different from the one I was two years ago is his guidance and effort. I would like to extend my sincere thanks to Dr. Emine Hande Cingil Tan for her insightful comments and suggestions. I am grateful to her for listening to me, motivating me when I needed it, and sharing her knowledge. I very much appreciate Assist. Prof. Eda Goldenberg and Dr. Hasan Yıldırım for their experience and time that helped me to shape my experiments and methods, particularly in the beginning of my Masters. I would also like to show gratitude to Dr. Selim Tanrıseven, Ali Osman Çetinkaya and Süleyman Çelik for sharing their instrumental knowledge with me. I'd like to acknowledge Semih Pehlivan for his helpful advice and support in conducting my experiments. I would like to thank my lab team Yelda Yorulmaz, Dr. Rana Golshaei and Gizem Beliktay for their precious help and support inside and outside the lab. I want to give my deep appreciation to A. Alp Yetisgin for discussing everything with me, sharing his opinion, for the devices he taught, and for being beside me.

Finally, I would like to express my gratitude to my mother Selma Mitmit; father Galip Mitmit and sister Selen Mitmit. I am grateful for their unconditional love, support and belief.

TABLE OF CONTENTS

LIST OF TABLES

LIST OF FIGURES

LIST OF ABBREVIATIONS

Abbreviation	Definition
IR	infrared
UV	ultraviolet
NIR	near-infrared
FTIR	Fourier-Transform infrared
ATR	attenuated total reflectance
TMM	transfer matrix method
NEP	noise equivalent power
ABV	alcohol by volume
DC	direct current
E	electric field
B	magnetic field
RF	radio frequency
pNIPAM	poly(*N*-isopropylacrylamide)
LCST	low critical solution temperature
OMO	oxide-metal-oxide
DHW	double-half wave
PVD	physical vapor deposition
PET	polyethylene terephthalate
AIBN	azoisobutyronitrile
THF	tetrahydrofuran
Al_2O_3	aluminium oxide
Ge	germanium
ZnO	zinc oxide
CO_2	carbon dioxide
YSZ	yttria-stabilized zirconia
VO_2	vanadium dioxide
AlN	aluminium nitride
Ag	silver
ITO	indium tin oxide

CHAPTER 1

1. Introduction

Over the years, researchers have conducted many studies on single and multilayer coatings theoretically and experimentally to create functionalities by carefully selecting matching materials. Various techniques can produce these coatings, including physical vapor deposition, chemical vapor deposition, spin coating, and atomic layer deposition. Typically, these coatings are thin, and the thicknesses are in the nanoscale.

Functional coatings and multilayer structures have a variety of applications. The aircraft industry can benefit from these functional coatings for many different purposes. For example, a nose cone controls the adjustment of airflow direction and stability in the plane. However, the nose cone can be affected easily by ice formation. Recently, scientists have developed a superhydrophobic anti-icing multilayer structure with periodic micro-nano structures on stainless steel [1]. Also, the insulation of nickel-based turbine blades of aircraft engines is crucial because they are subjected to elevated temperatures during operation. High-temperature insulation can be achieved by coating 4-layer Yttria-stabilized zirconia (YSZ) and aluminum oxide (Al_2O_3) structure [2]. While aircraft engine compressor blade requires high erosion resistance, compressor blades working in the marine or acidic environment requires good corrosion resistance. Multilayered CrAlTiN-AlTiN and CrAlTiN-CrN can increase erosion and corrosion resistance, respectively [3]. Also, it is common to use functional coatings for different sensing applications. For example, ZnO, an n-type semiconductor, has high stability in a toxic-environment. It is sensitive to CO_2 gas, depending on the operation temperature and thin film thickness [4]. Furthermore, coatings can serve as energy-saving materials in our daily life. Air conditioning and cooling expenses in buildings can be reduced by controlling the total heat transfer inwards and outwards of a building. Windows coated with low-E coatings can reflect most solar heat on hot days and retain heat inside the building on cold days.

While blocking the heat, the coatings allow transmittance in the visible light that is well suited for a window application. Due to high reflectance properties, conventional low-E coatings consist of a very thin silver layer and dielectric multilayers. However, various new studies exist in the literature to show an alternative to the thin silver layer, such as the use of aluminum nitride (AlN) [5] for air-stability of the window and integration of vanadium dioxide (VO_2) [6] film to increase luminous transmittance.

By adjusting the layer thickness and the material properties of the individual layers in a multilayer structure, the optical filters can reflect or transmit light in the desired intensity and wavelength range. The optical filters generally consist of 2 types. Those made by focusing on dielectric/dielectric layers are designed to maximize transmission or reflection. Those combining metal/dielectric layers are produced to achieve spectral selectivity [7]–[9] or the required sheet resistance [10]. Reflective filters have been developed for various applications such as passive radiative cooling [11], solar reflection [12], display [13], [14], and enhancement of laser beam power[15]. Whereas transmission filters are developed for optical sensors [16], high-resolution imaging [17], and gas-sensing applications [18]. This thesis consists of three main chapters. In the first chapter, the thesis gives information about the light-matter relationship, the theory, production, and characterization of multilayer coatings. The second chapter describes the design, fabrication, and characterization of a multilayer bandpass filter and lithium tantalate ($LiTaO_3$) pyroelectric detector. The 7-layer mid-infrared bandpass filter, which has a center wavelength of 3.2 μm and bandwidth of ±232 nm, is produced by alternating Ge and Al_2O_3 layers. We developed an optical gas detection setup by combining the bandpass filter and the pyroelectric detector. In the presence of ethanol in the measuring setup, the detector shows a sensitive response to a change in temperature and induces a voltage change. Therefore, we show that the optical gas detection system can detect and quantify various ethanol concentrations (6% - 100% by volume), including alcoholic beverages like beer and wine. Such a detection system shows the potential to detect other gas molecules just by changing the bandpass filter that only overlaps with the vibrational absorption mode of the target gas.

The third chapter describes the development of a smart window that shows three functionalities; passive visible light modulation, on-demand visible light modulation, and broadband infrared light reflection. To construct the smart window, we prepare two materials. First, a heat-responsive material, poly-NIPAM, is synthesized via radical

polymerization. Secondly, we produce a transparent heater from an oxide-metal-oxide (OMO) multilayer structure. The materials are combined where the thermoresponsive layer is placed between the transparent heater and plexiglass. We show that the smart window can modulate the visible light when the environment temperature reaches the lower critical solution temperature at 32.5 °C. At this temperature, the thermoresponsive layer changes from the transparent state to the opaque state, attributed to the change in the polymer structure. In this transition, the smart window blocks the outdoor heat. Users can activate the window's opacity on-demand when the environment cools down at night by activating the transparent heater. Thus, ensuring privacy protection for the users. The smart window can also be used in colder countries because the window can reflect generated heat indoors to maintain a comfortable temperature. The combined functionalities of this smart window can be a solution to reduce energy consumption for space heating and cooling.

1.1. Theoretical Information

1.1.1. Optical Constants and Complex Refractive Index

The refractive index defines the bending or refracting ratio when light enters a material. That can be explained by Snell's law of refraction in the following equation 1 [19].

$$n_1\theta_1 = n_2\theta_2 \quad (1)$$

The reflection at the surface of the medium and the absorption in the medium depend on a magnitude called the complex refractive index. It is denoted by the symbol $\underline{n}$ and expressed by the following equation 2.

$$\underline{n} = n \pm i\kappa \quad (2)$$

In the equation above, n is the real part of the refractive index and indicates the phase velocity, while the imaginary part κ is called the extinction/absorption coefficient — although κ can also refer to the mass attenuation coefficient— and indicates the amount of attenuation when the electromagnetic wave propagates through the material.

Alternatively, we can describe a material's optical properties by a complex dielectric function, as seen in equation 3.

$$\varepsilon = \varepsilon_1 \pm i\varepsilon_2 \quad (3)$$

The relation between the complex refractive index and the complex dielectric function can be described as follows.

$$\varepsilon = \underline{n}^2 \quad (4)$$

In the complex refractive index, n and k explain how a light wave is influenced by material. In the dielectric function, ε_1 and ε_2 explain how the light wave influences the material.

1.1.2. Interference in Thin Film and Multilayer Structure

Interference is the main principle of thin films. When a light wave hits the thin film material, it is reflected from both boundaries, as shown in figure 1A. This phenomenon can be explained by the Fresnel equation. The light beam that meets the film at the air-film interface splits into two by reflecting and propagating through the film. The light beam that refracts from point A and enters the film undergoes a second reflection at the film-substrate interface (from point B). The beam then leaves the film at point C. Rays reflected from both surfaces travel parallel to each other. Internal reflections continue between surfaces until a certain part of the beam loses its intensity in the film. If the refractive index of the thin film material is greater than the refractive index of the medium from which the wave originates, a 180° phase shift occurs in the reflected wave. If the refractive index of the medium from which the wave originates is greater than the refractive index of the thin film material, n, no phase shift will occur in the reflected wave [20]. Depending on the phase of these reflected waves, constructive or destructive interference occurs. Constructive interference causes reflection to increase, while destructive interference causes reflection to decrease. The desired reflection and transmission ratios depend on the phase difference, namely the refractive index and the film thickness [21].

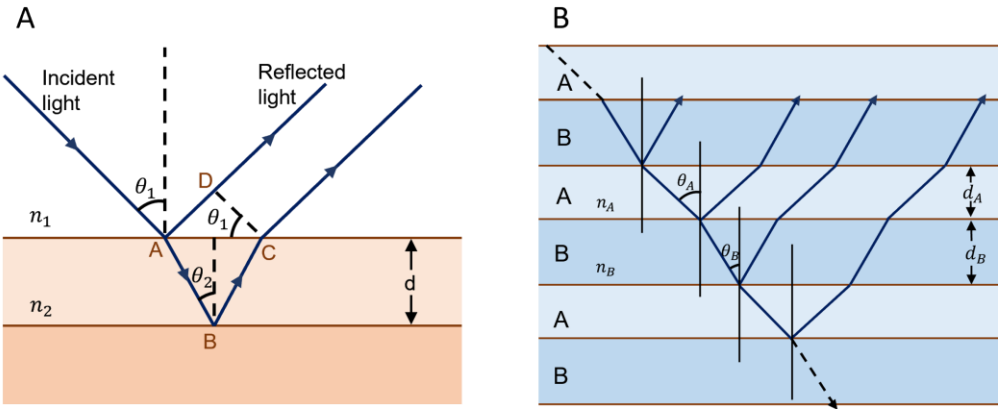

Figure 1. A) Interference in a thin film. B) Interference in a multilayered structure.

Interference in multilayered structures is similar to interference in thin-film materials; light waves are reflected at each boundary in multilayered structures. A multilayered thin-film structure is shown in Figure 1B. The refractive index of material B used here is greater than that of material A ($n_A < n_B$). In this case, while a 180° phase change occurs at each A-B boundary, there is no phase change at B-A boundaries. At the low refractive index layer surface, no phase shift occurs in refraction or reflection. Half-wavelength phase shift occurs in reflection at the surface of the layer with a high refractive index. Equations 5 and 6 show the necessary conditions for constructive interference and maximum reflection, respectively [22].

$$2(n_A d_A Cos\theta_A + n_B d_B Cos\theta_B) = m\lambda \quad (5)$$

$$2n_A d_A Cos\theta_A = (m' - 1/2)\lambda \quad (6)$$

In Equations 5 and 6, d_A and d_B are the thickness (m) of the A and B thin films; n_A and n_B are the refractive indices of the thin films; θ_A and, θ_B are the angle (degrees) of the incident wave at the lower boundary of the A and B thin films; λ is the wavelength of the light.

Multilayer structures can be built with various techniques. The transfer matrix method (TMM) is based on Maxwell's equations and analyzes the propagation of an electromagnetic wave or an acoustic wave through a layered medium. Accordingly, there are simple continuity conditions for the electric field along boundaries from one medium to another. If the field is known at the beginning of a layer, the area at the end of the layer can be obtained with the help of a matrix operation. A multilayered stack can also be represented as a system matrix that is the product of individual layer matrices [23].

OpenFilters is an open-source software that Stéphane Larouche and Ludvik Martinu developed to design and simulate optical structures. The software uses a matrix approach to calculate and simulate the multilayer structures [24]. Generally, it is challenging to design a multilayer thin film precisely. However, *OpenFilters* can optimize the desired structure by changing layer thicknesses according to user-defined targets. We use *OpenFilters* software to design, optimize and simulate our multilayer thin films. The success of the software in designing optical filters also depends on the user. The user should guide the software at the beginning by entering the optical constants of layer materials, defining the number of layers and their initial thicknesses. To be able to define all these, the theory behind the multilayer structure should be known. The following sections will explain the design theory of two different multilayer structures used in the thesis.

1.1.3. Bandpass Filters

Several types of multilayer structures exist for different purposes, such as anti-reflection coatings, mirrors, and bandpass filters. Depending on the arrangement of the layers, the number of layers, optical constants, substrate, and material properties, there are many possibilities to achieve the desired optical component. For example, a simple anti-reflective coating should consist of a single film that has a refractive index equal to the square root of the substrate, and its optical thickness should be one-quarter of a wavelength. Another fundamental type of thin-film structure is a stack of alternate high- and low-refractive-index layers with quarter-wavelength thicknesses. In this structure, the phase shift on reflected light will not occur within the high index material, while the reflected light within the low index material will shift 180°. This assembly is the basic structure of high-reflectance coatings and can make the reflection as high as possible by increasing the number of layers. After the construction of these coatings, it was observed that the high reflectance is limited to a certain wavelength range while the reflectance on the other wavelengths is quite low, which allows for the design of thin film optical filters such as long-wavelength pass, short-wavelength pass, band-pass and Fabry-Perot filters [25].

A filter that allows transmission for a selected range of wavelengths and rejects the others is known as a bandpass filter. We use a technique that combines shortwave-pass and longwave-pass filters to design a bandpass filter with a customized range. By combining

these filters that have transmittance at different ranges on the spectrum, a bandpass filter can be obtained, as shown in figure 2. Either we can coat these two filters on the opposite sides of the substrate or add them up on the same side of the substrate. The structure of the filter can be represented as *Air/(Longwave-pass)/Substrate/(Shortwave-pass)/Air* or *Air/Substrate/(Longwave-pass)/(Shortwave-pass)/Air* where longwave-pass and shortwave-pass are N-fold periodic replication of high and low index materials that can also be shown as $(HL)^N$.

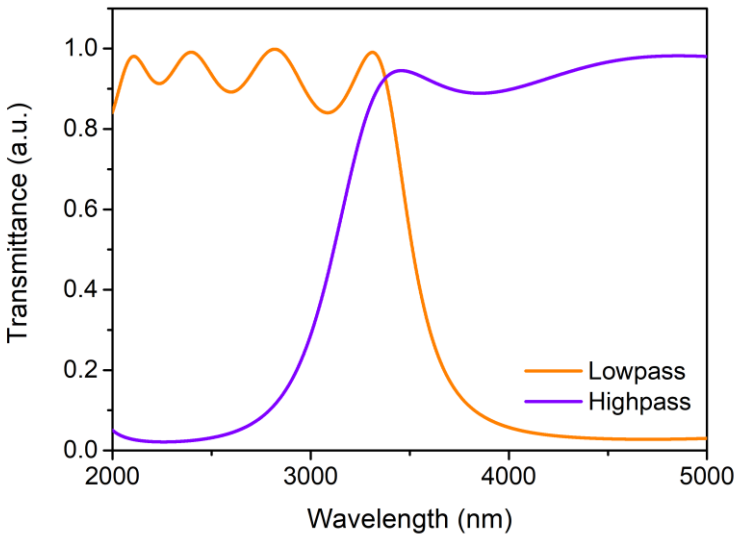

Figure 2. Combination of longwave pass (highpass) and shortwave pass (lowpass) filters designed in OpenFilters Software.

If a narrow bandpass filter [26] is desired, a thin film Fabry-Perot resonator is well-suited for the purpose. The Fabry-Perot filter consists of a dielectric spacer (optical cavity) layer that usually has a half-wavelength thickness, confined by two high reflectance coatings (Figure 3) [25]. Due to the placement of an optical cavity between two reflective coatings, light interference occurs between the multiple reflections. If the transmitted beams are in phase, maximum transmittance is obtained as a result of constructive interference. Conventionally, reflecting layers are metallic, but the structure can be designed as all-dielectric. The symbolic representation of the single-cavity Fabry-Perot structure is *Air/Substrate/*$(HL)^N$*/LL/*$(HL)^N$*/Air* when the medium is the air. A single-cavity Fabry-Perot filter has a triangle transmittance structure, and the filter can be further developed by adding more cavities. The combination of two cavities is known as double-cavity or double-halfwave filter (DHW), and it is represented as *Air/Substrate/*$(HL)^N$*/LL/*$(HL)^N$*/ LL/*$(HL)^N$*/Air*. The number of optical cavities can be increased to triple-halfwave (THW)

by adding one more cavity to DHW, which will result in similar bandwidth as DHW but with steeper sides.

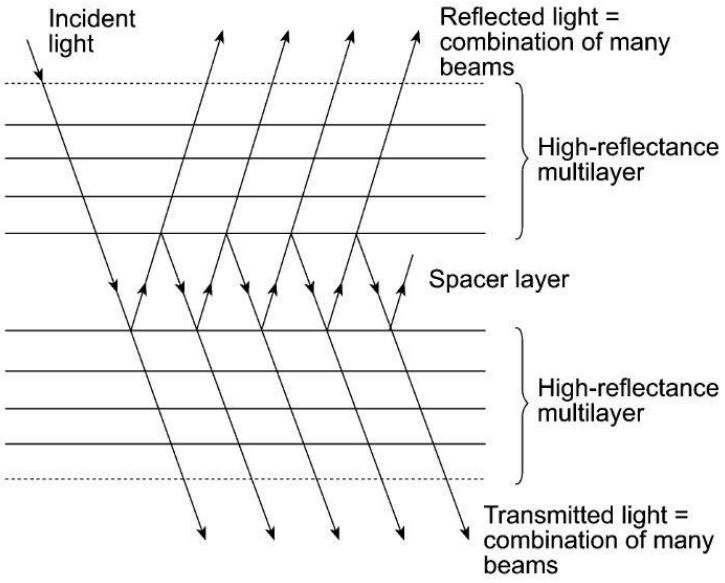

Figure 3. Structure of the Fabry-Perot filter [23].

The increase in layer thickness is required to achieve transmittance in higher wavelengths according to the quarter wavelength theory. However, thicker coatings can cause problems such as reduced transmittance intensity and thermal stress accumulation. Substrates with significant mismatch coefficients of thermal expansion (CTE) with the deposited coating materials can induce crack formation due to residual stress on coating. The problems can be resolved by selecting the appropriate layer materials suitable for the electromagnetic region of interest while maintaining a good CTE match. For instance, selecting high- and low-index materials with large differences in their refractive indices can prevent stress accumulation and exfoliation by decreasing the overall thickness. Germanium, Ge (n~4) as high-index and aluminum oxide Al_2O_3 (n~1.6) [27] as low-index materials are a good pair of materials for the mid-IR region.

1.1.4. Design of Transparent Resistive Heaters

A transparent conductive electrode (TCE) is essential for devices such as thin-film solar cells, light-emitting diodes, flat-panel displays, touchscreens, and electrochromic devices. The OMO structure is suitable for transparent heater design because it allows us to optimize electrical conductance and optical transmittance at the same time. Since the resistivity of the OMO electrode is dominated by electron transport in the ultra-thin metal

layer that is sandwiched between the top and bottom oxide films in the OMO electrode, the material type and morphology of the ultra-thin metal layer are crucial parameters to ensure a high electrical conductance. The increase in thickness of the metal layer will decrease the resistance. However, the transmittance will decrease dramatically due to increased interaction between the photons and free electrons in the metal layer. Therefore, an ultrathin metal layer of mostly less than 10 nm should be coated to overcome this situation. The deposited metals are inclined to coalescence and make island-like structures in the early stages of growth. A supporting oxide layer that will be coated on the bottom can support the homogenous growth of metals. Moreover, an oxide layer on top can protect the metal layer and enhance the transmittance of the overall structure to the longer wavelength range [28].

1.2. Fabrication Techniques

Different deposition techniques can obtain the required properties of the thin film and modifications of the existing properties [29]. There are numerous deposition techniques, but since this thesis focuses on thin film deposition for forming nanometer-sized layers, priority will be given to the two major deposition techniques, particularly the sputtering and e-beam evaporation techniques we used for coating deposition in the thesis studies. The techniques used are sub-branches of the physical vapor deposition (PVD) method. The physical vapor deposition (PVD) method removes atoms from the material's surface and deposits them on the substrate in a high-vacuum chamber. The thickness of the films produced from these methods can be controlled from a few nanometers to micrometers. Coating speed may vary with applied voltage or temperature.

1.2.1. Sputtering

In the sputtering technique, ionized atoms are bombarded on the target material, and the atoms detached from the target material are accumulated onto the substrate, thus, forming a thin coating. Argon gas is generally preferred in a sputtering system because it is both inert and cheap. The operating scheme of the sputtering system is shown in figure 4A. Various sputtering techniques exist in the literature, and their names are given based on the source and the orientation of the process. The techniques are diode sputtering (cathode or radio frequency), reactive sputtering, bias sputtering, magnetron sputtering, and ion-beam sputtering [30]. Depending on the power sources, two common types of sputtering are available.

DC sputtering is one of them, and it has planar electrodes (anode and cathode). The target material is placed on the cathode, and the substrate is located at the anode. Argon gas is preferred over neon and helium gases because its higher mass creates more energetic collisions with the target. While the target, which is the source of the material to be coated, is placed on the cathode, the substrate to be coated is placed on the anode. A high DC voltage is applied between the cathode and the anode to maintain glow discharge (current flow). As a result of the glow discharge, the gaseous ions are accelerated through the target material, and sputtering occurs from the target. The sputtered target material is deposited on the substrate, thus forming a thin layer. Generally, the target material should be metal or highly conductive for DC sputtering because only a conductive material can maintain glow discharge between the electrodes [29], [31].

To overcome the conductivity requirement of the target material, RF (radio frequency) sputtering is used for non-conductive materials. The electrical potential of the current is alternating in the vacuum atmosphere at radio frequencies to avoid charge building up on the target material. A blocking capacitor is placed between the cathode and the anode, and they are connected in series. The capacitor helps the power transfer from the RF source to the plasma discharge. The cathode is bombarded with a high voltage at a fixed frequency of 13.56 MHz in a vacuum atmosphere. This bombardment causes the high-energy ions to sputter the atoms, and the sputtered atoms are coated onto the substrate as a thin layer [32], [33].

As a result of ion bombardment, secondary electrons are emitted from the target material during the sputtering process. Restricting these electrons' movements can increase the process's efficiency. Therefore, magnetron sputtering was developed to achieve higher deposition rates, high ionization efficiency in plasma, and overcome substrate heating effects. The magnetron sputtering system uses a magnetic field positioned parallel to the target surface, limiting secondary electron movement around the target [34], [35].

1.2.2. E-beam Evaporation

The evaporation of source material in a vacuum chamber using high-energy electrons in the form of an intense beam is called electron beam evaporation. The schematic of the e-beam evaporation system is shown in figure 4B. This method is advantageous as it allows the evaporation of materials with high melting temperatures (up to 4000 °C). A hot filament causes thermionic electron emission [36] and the resulting electrons are

accelerated and directed with the help of a magnetic field. The magnetic field also allows evaporation induced by the sweeping motion of the electron beam, thus enabling uniform evaporation of the source material. A homogenous coating thickness on the substrate can be obtained by rotating the substrate holder. In addition, different reactive gases can be supplied to the chamber to react with gaseous target material to coat a mixture of compounds on the substrate.

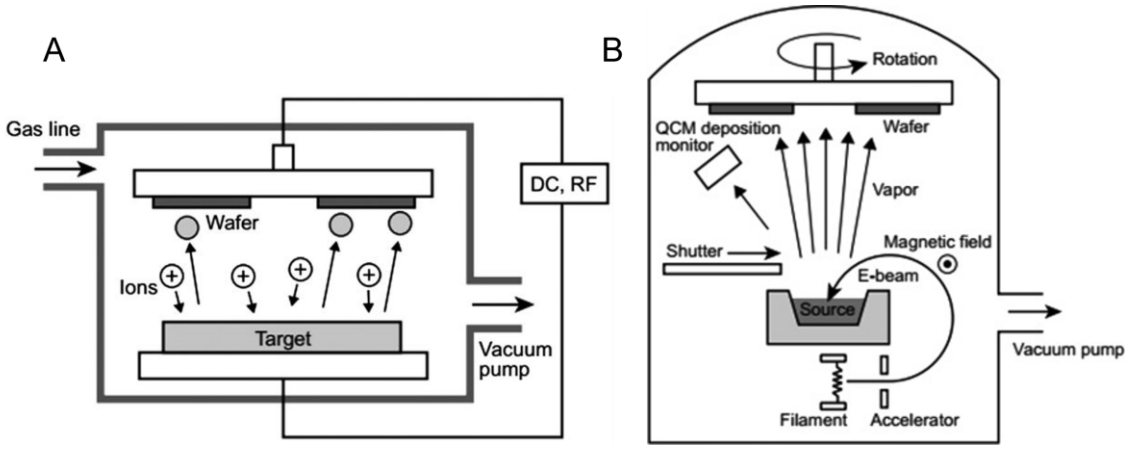

Figure 4. A) Schematic representation of sputtering process. B) Schematic of e-beam evaporation system. Reprinted from John X.J. Zhang, Kazunori Hoshino, Fundamentals of nano/microfabrication and scale effect, in: Molecular Sensors and Nanodevices, 2019, pp. 43–111, with permission from Elsevier [37].

1.3. Characterization of Thin Films by Ellipsometry

There are several common methods to determine thickness, such as calipers, micrometers, and yardsticks. However, these techniques are not useful when the thickness of the film is thinner than a micrometer. Also, techniques of interferometry (where intensity is the measured quantity) are ineffective for thicknesses lower than several thousand angstroms [38]. On the contrary, ellipsometry is a useful technique for film thicknesses from several micrometers to sub-nanometer. The primary working principle of ellipsometry is derived from polarized light. A linear light beam with p- and s- polarization components is directed to the sample of interest, and reflected light from the sample is detected. In other words, ellipsometry measures the change in the polarization state of p- and s- components of the incident light beam after being reflected from the sample. The change in polarization is denoted as an amplitude ratio, Ψ, and a phase difference, Δ. The response from the measurement depends on the thickness and the optical properties of the thin film. Other material properties associated with a change in optical response, such as the doping

concentration, crystallinity, surface roughness, and composition, can also be characterized.

In 1864, Maxwell proposed a theory that light is an electromagnetic wave and can be explained with *Maxwell's Equations.* According to the theory, the electromagnetic wave is not an actual material, but instead, it is both an electric field (E) and a magnetic field (B). The vector fields, E and B, are perpendicular to each other, while both are perpendicular to the direction of propagation. In an ellipsometric measurement, only the vibrations of the electrical field is considered [38], [39]. The geometric orientation of an electric field in space and time depending on the direction of its propagation is called polarization. A light that has random orientation and phase is described as unpolarized light. Light following a specific path, orientation, and phase can be considered polarized. Figures 5A, B, and C represent the linear, circular and elliptical polarized light according to a z- direction of propagation. Elliptical polarization is defined by the orthogonal waves with arbitrary amplitude and phase, and ellipsometry utilizes elliptical polarization.

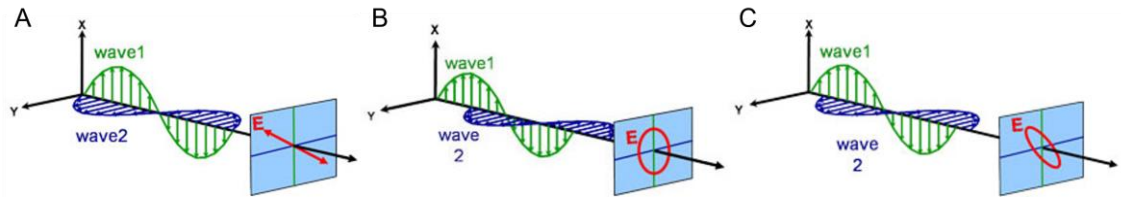

Figure 5. Combination of orthogonal waves for demonstration of A) linear B) circular C) elliptical polarization [39].

When linearly polarized light is directed to a surface, it will reflect from the surface as orthogonal waves with arbitrary amplitude and phase. In other words, the reflected light is elliptically polarized. The change in polarization depends on the interaction of light with the sample, where sample parameters such as optical constants, film thickness, and the number of layers can affect the change. Ellipsometry measures this polarization change to determine the optical properties of the sample. Figure 6 shows the measurement principle of ellipsometry.

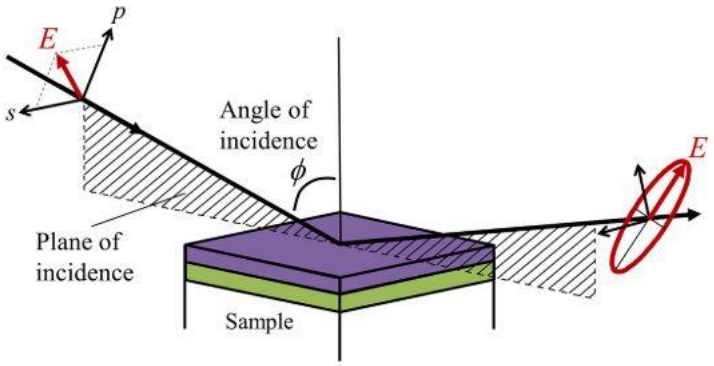

Figure 6. Demonstration of the ellipsometry measurement [38].

Electric fields parallel and perpendicular to the plane of incidence are called p- and s-polarized, respectively. Primarily, ellipsometry measures s- and p- polarization change upon reflectance or transmittance after the interaction of light with a sample. This phenomenon can be described with the following equation,

$$\rho = \frac{R_p}{R_s} = tan\psi\, e^{\Delta i} \quad (7)$$

In equation 7, rho (ρ) is a complex number; R_p and R_s are the reflectivities of p- and s-polarized light, respectively; and the ellipsometric parameters $tan\psi$ is the magnitude of the reflectivity ratio and Δ is the phase.

The interference, which is mentioned in section 1.1.2, contains both amplitude and phase information [40]. Depending on the film thickness and optical constants, constructive and destructive interference occurs and thus affects the phase (Δ) and magnitude (ψ). Figure 7A and 7B show spectroscopic ellipsometry measurements of 70 nm and 247 nm germanium coating between 200-1000 nm wavelengths and at 75° incidence angle, respectively. The phase (Δ) is very sensitive to the coating thickness and can be observed from the comparison of phases in Figures 7A and 7B. The path length of light traveling through the film is determined by thickness, while the refractive indexes determine the velocity of light waves and the angle of refraction. Therefore thickness measurements are dependent on the optical constants [41].

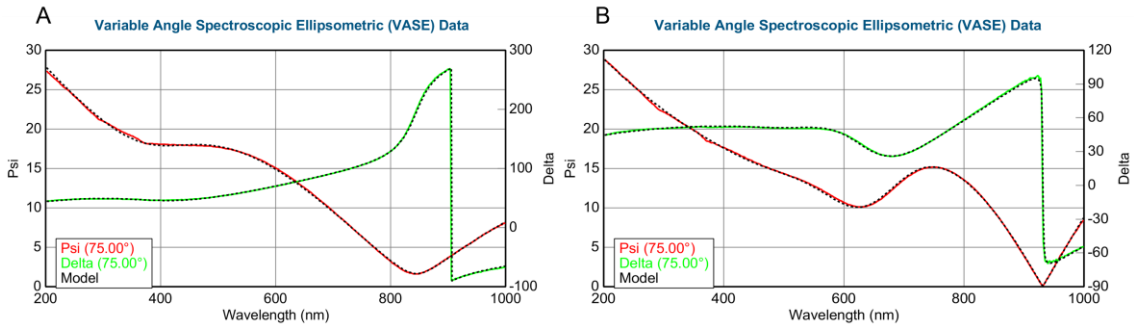

Figure 7. Ellipsometry measurement of A) 70 B) 247 nm germanium thin film.

The material's optical constants change as a function of the wavelength. Moreover, the optical constants affect the optical properties (transmittance, reflectance, absorbance) of the coating or thin film. Therefore, each material has unique light transmittance and absorbance within a specific wavelength range depending on its optical properties. The ellipsometric measurements taken depending on the material's transmittance or absorbing wavelength range should be modeled with a suitable dispersion relation for that range. Modeling is done by fitting the ellipsometric measurement to the appropriate dispersion relation, such as Cauchy, Sellmeier, and Lorentz. The measurement should be fitted to a correct model and in the correct wavelength range to determine the optical constants. The following two sections discuss the various models fitting for transparent and absorbing layers in the 400 – 1000 nm wavelength range.

1.3.1. Modeling of Transparent Films

Refractive indexes increase when the wavelength decreases for all transparent coatings and films. This phenomenon can be referred to as normal dispersion. Two dispersion relations that are typically used to describe the refractive indices of transparent and dielectric materials are Sellmeier and Cauchy. Cauchy relation is a simplified version of Sellmeier and can be applied in the spectral region that is far from the absorption region of the coating [42]. Equation 8 describes the Cauchy dispersion relation.

$$n = A + \frac{B}{\lambda^2} + \frac{C}{\lambda^4} \quad (8)$$

A, B, and C are Cauchy coefficients that describe the real part of the refractive index. Figure 8 shows a typical refractive index curve for a transparent dielectric thin film modeled using the Cauchy dispersion relation.

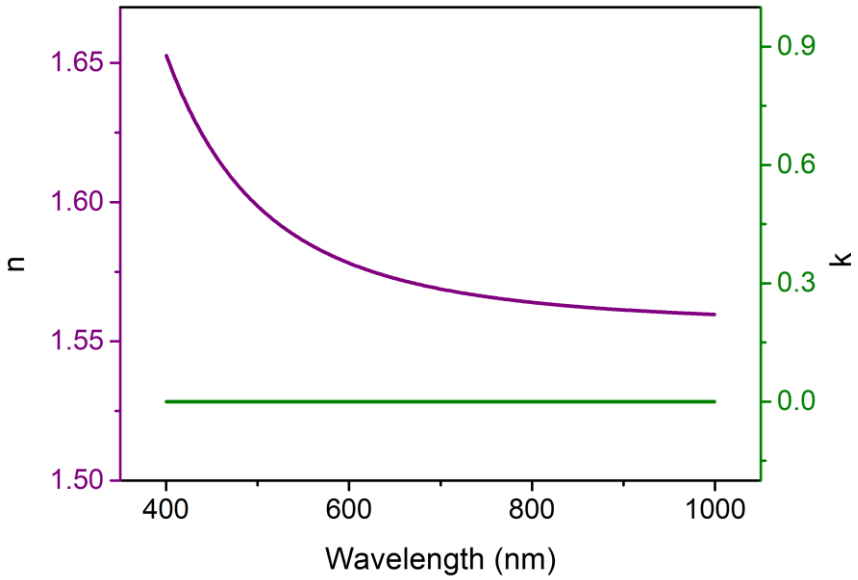

Figure 8. Optical constants of SiO layer.

In its original form, the Cauchy relation assumes that k is 0. Nevertheless, the relation can be modified for materials that have slight absorption in the UV range by adding the relation of extinction coefficient (k). As described below (equation 9), the Urbach equation models the extinction coefficient for small absorption features [43].

$$k(\lambda) = A_k e^{B_k(E-E_b)} \quad (9)$$

In equation 9, E is the photon energy, and E_b is the $1240/\lambda_b$. λ_b is suggested to set to a value that is near to the shortest wavelength range by the analyst where A_k and B_k can vary. However, this relation cannot be used for highly absorbing materials.

1.3.2. Modeling of Absorbing Films

The absorbing materials often have transparent regions in electromagnetic spectra that can be modeled with Cauchy or Sellmeier equations. Refractive indexes in the absorbing regions can be modeled using either the oscillator theory or B-Spline interpolation, depending on the complexity of the thin film. B-spline is preferred to describe more complex functions in a multilayered structure, while the oscillator model is preferred for a low number of layers. The general shape of a material's refractive indices in the absorbing range is such that there are peaks in absorption at resonant frequencies where the material is most likely to absorb incident light of that wavelength. If a sample has unknown refractive indexes or has both absorbing and transparent regions in the

measurement, B-Spline can be a good choice because it allows flexibility while modeling the refractive indexes. The oscillator theory is generally explained by complex dielectric function because the oscillator shapes(Figure 9A) are based on how a material reacts to the incoming electromagnetic wave. Moreover, it is common to use the x-scale as a function of frequency (photon-energy) instead of wavelength. Many dispersion relations use oscillator theory to model absorption, including Lorentz, Harmonic, and Gaussian [44]. Firstly, the imaginary part of the refractive index is described by the oscillator. Then, Kramers-Kronig consistency is used to create the shape of the real part while modeling the absorbing films. All oscillators have similar features such as amplitude, broadening, and center energy. The equation for the Lorentz oscillator is written as shown in equation 10 as an example.

$$\varepsilon = \varepsilon_{1\,offset} + \frac{AE_C}{{E_C}^2 - E^2 - iBE} \quad (10)$$

where A, B, and E_C are the amplitude, broadening, and center energy, respectively. E is the photon energy (eV).

ε_2 is described by the center energy, amplitude, and broadening of the resonant absorption with a Gaussian oscillator, as shown in Figure 9A. The difference between the Gaussian and Lorentz oscillators is shown in figure 9B by plotting ε_2 as a function of the photon energy. It can be seen that Gaussian approaches zero faster than Lorentz.

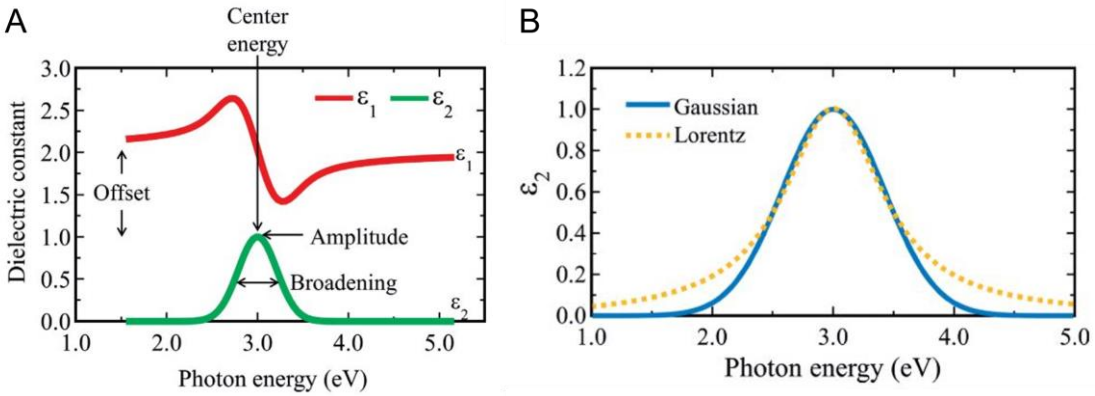

Figure 9. A) A single Gaussian oscillator B) Comparison of Gaussian and Lorentz oscillators [38].

Both of the curves are symmetric. However, a material with a bandgap and no absorption behavior below that bandgap energy can be modeled by using asymmetric oscillators such as Tauc-Lorentz and Cody-Lorentz. These oscillators are common to model amorphous dielectrics and semiconductors [38], [45]. The main difference between these two oscillators stemmed from modeling absorption at energies slightly higher than bandgap. While the Tauc-Lorentz follows the Tauc law shown in equation 11, Cody-Lorentz is shown in equation 12, where E_g is the band gap energy. Also, it is possible to add an Urbach tail to the Cody-Lorentz for small absorption behavior at the energies below the band gap [44].

$$\varepsilon_2(E) \propto \frac{\left(E - E_g\right)^2}{E^2} \quad (11)$$

$$\varepsilon_2(E) \propto \left(E - E_g\right)^2 \quad (12)$$

The imaginary part versus photon energy plots for Tauc-Lorentz and Cody-Lorentz oscillators are shown in Figures 10A and 10B, respectively.

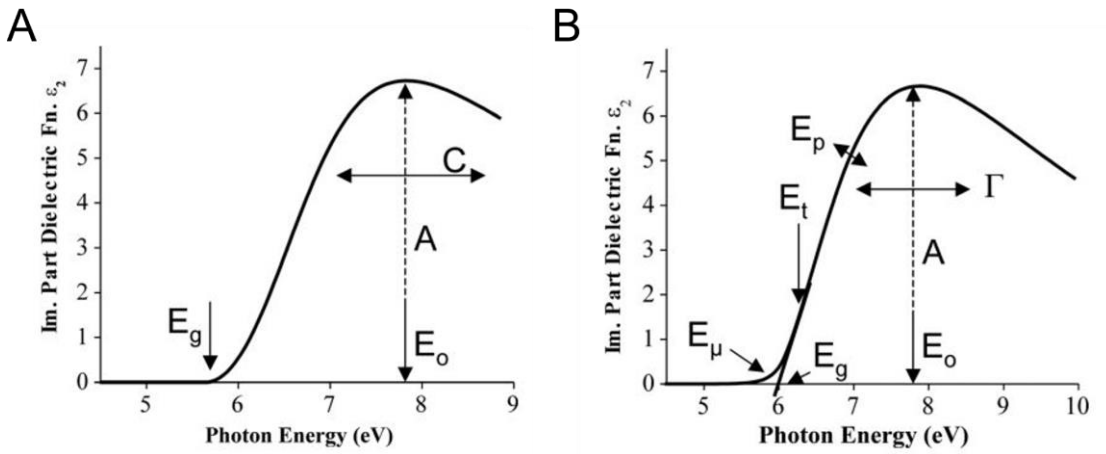

Figure 10. Model of A) Tauc-Lorentz B) Cody-Lorentz for the imaginary part of the dielectric function of HfO_2 [46].

The chapter is in preparation for submission to ACS Sensors.

CHAPTER 2

2. Identifying and Quantifying Alcohol in Beverages with Pyroelectricity

2.1. Aim of the Study

Ethanol is one of the immense organic chemicals used in industrial and consumer goods. It is the only type of alcohol that is safe for consumption. The alcohol amount in alcoholic beverages is indicated as alcohol by volume (ABV). It is crucial to identify and quantify the alcohol content due to strict regulations as the amount of alcohol consumed directly affects the body. We combine a customized optical bandpass filter centered at 3250 ± 232 nm and a 60 µm thick $LiTaO_3$-based pyroelectric detector in a non-dispersive infrared gas detection system to detect and quantify ethanol of different concentrations. The bandpass filter fabricated using e-beam evaporation systems consists of alternating high and low refractive index layers, Ge and Al_2O_3, respectively. In the presence of ethanol in the gas cell and the bandpass filter placed in the light path between the broadband infrared light source and the pyroelectric detector, the detection system shows a voltage signal drop attributed to the pyroelectric effect. This electronic response occurs when light is absorbed by the ethanol molecules, thus changing the temperature. As the ethanol concentration increases from 6% to 100%, the difference in signal change increase from 0.1 V to 0.8 V. We also show that the measurement system can detect and quantify alcoholic beverages such as beer (6% ABV) and wine (13% ABV). Notably, a complete detection can be done in just under 2 minutes.

2.2. Introduction

Monitoring of alcohol and its concentration for numerous industrial processes to produce alcoholic beverages [47], [48], food[49], cosmetic, and pharmaceutical products [50] are

becoming important due to stringent regulations and increasing health concerns. Analytical methods to determine the concentration of alcohol must be reliable and accurate to control the fermentation process and accurate labeling of alcohol content on a package. Hydrometers and refractometers are often used in the brewery industry to obtain quick measurements of the alcohol content. However, this method depends on the operator's expertise and determines the alcohol content indirectly by measuring the sugar content [51]. Liquid chromatography technique, which is the "gold" standard for ethanol testing, is too expensive, slow, and requires a laboratory. Such a method is only suitable for bigger companies [52]. Another alternative method to determine alcohol content in a food process and alcoholic beverages is an optical-based sensor. This method utilizes the mid-infrared (MIR) spectral region between 2-25 μm that is part of the electromagnetic spectrum where a vast array of molecules exhibits strong characteristic vibrational absorption modes. Such a method is suitable for the detection of ethanol due to the distinct absorption peaks in the region 3367 – 3449 nm (2899 – 2970 cm^{-1}) attributed to the CH stretching of the molecule. Given the scalability of this method to detect different molecules, there is considerable interest in the method due to this "molecular fingerprint" region where vibrational and rotational characteristics of molecules can be distinguished to identify and quantify the molecule of interest unambiguously [53], [54]. With the emerging trend of consumer electronics and sensors for the internet of things (IoT), optical gas sensors are becoming popular for use in chemical analysis applications such as air quality monitoring [55], [56], medical diagnosis [57], [58], and industrial and food process control [59]. Therefore, optical gas sensors like the non-dispersive infrared (NDIR) gas sensor has advantages due to the selective detection based on the characteristic vibrational absorption wavelength [56], high sensitivity [60], and fast response time [61]. Like most optical sensors, an NDIR gas sensor comprises a broadband light source that encompasses the MIR wavelength, a certain length of gas cell that allows light to interact with the gas of interest, a narrowband optical filter that overlaps with the characteristic absorption wavelength of the gas target, and an optical detector to detect the absorbed wavelength of the light beam.

In this work, we propose an NDIR gas detection system by fabricating MIR multi-layer bandpass filter and $LiTaO_3$ pyroelectric detector. For the multilayer bandpass filter, we show how we realize the design and fabrication of this optical component. Optical multi-layer filter generally consists of 2 types of materials: materials focusing on

dielectric/dielectric layers are designed to maximize transmission or reflection, and materials focusing on dielectric/metal are designed to emphasize broad and narrow spectral selectivity for reflectance and absorption [62], [63]. The former option was chosen to achieve high transmittance in a selected wavelength region. Various materials which are transparent in the MIR range have been used to design optical filters, including germanium (Ge) and zinc sulfide (ZnS) [64], [65], niobium pentoxide (Nb_2O_5) [66], silicon monoxide (SiO) [67], and aluminum oxide (Al_2O_3) [68]. Among these materials, we used Ge and Al_2O_3 to fabricate the multi-layer bandpass filter due to the large difference in the refractive indices between Ge and Al_2O_3 ($\Delta n > 2$), which reduces coating stress accumulation [68], thermal stress mismatch, and reduces the number of layers to achieve the desired spectral selectivity [69]. In addition, the high transmittance intensity in the MIR for this pair of materials over other materials is highly desirable for our application [69].

Among the different optical detectors such as photodiode [66], [70], [71], thermopile [57], and pyroelectric [72]–[74], we chose to fabricate $LiTaO_3$ pyroelectric detector. Despite the disadvantages in sensitivity and responsivity, the pyroelectric detector has several advantages, including ease of fabrication, less expensive, wide spectral response, and operation in uncooled conditions [75]. Lithium tantalate ($LiTaO_3$) is an attractive material for the pyroelectric device because of its high chemical stability, high Curie temperature (620 °C), and it is insoluble in water. Due to its robust properties, the $LiTaO_3$ pyroelectric detector is used in various applications, including motion detection, flame detection, and broadband infrared sensor. The pyroelectric material undergoes spontaneous polarization and thermal expansion in its crystal lattice upon detection of temperature change. As a result, the pyroelectric effect induces a change in the detector's electronic signal [75]–[77]. We selected a z-cut, 60 ± 10 μm thick, 1 cm^2 area, lithium tantalate ($LiTaO_3$) as the pyroelectric material with 2.3×10^{-7} $C/cm^2/K$ pyroelectric coefficient (p). Coating electrodes on both sides of a z-cut $LiTaO_3$ substrate allows opposite charges to be collected onto the electrodes when the pyroelectric material detects a change in temperature. Thus, a current is generated and flows to the external circuit. The z-cut pyroelectric substrate is favorable for our application as the pyroelectric device can be fabricated in a layered manner and with the desirable active area [78]. Pyroelectric current (I_p) is proportional to the detector's active area (A), and the rate of change in temperature (dT/dt) as given in equation (13).

$$I_P = pA\frac{dT}{dt} \qquad (13)$$

We intend to prove in this work that pyroelectricity from $LiTaO_3$ can detect ethanol vapor of different concentrations and alcohol concentrations found in beverages like beer and red wine at room temperature. Notably, this proof of concept shows potential scalability for other applications which require the detection of gas targets that absorb at 3250 nm. This system can be improvised to detect other gas molecules by changing to another suitable bandpass filter to achieve the desired selectivity.

2.3. Materials

Aluminum oxide (Al_2O_3, 99.99%), germanium (Ge, 99.99%), chromium (Cr, 99.99%), sapphire substrate and Z-cut lithium tantalate ($LiTaO_3$) crystal were purchased from Maideli. Gold (Au, 99.9%), local beer, and local wine were purchased from local suppliers.

2.4. Methods

2.4.1. Development of the Multilayer Band-pass Filter

Single-layer Al_2O_3 and Ge thin coatings were deposited on a 0.3 mm thick polished Si substrate by e-beam evaporation at $4.2x10^{-6}$ mbar pressure and 0.15 nm s^{-1} deposition rate. These deposition parameters were kept constant for the coating deposition processes. The refractive indices of substrate and multilayer coating were measured by spectroscopic ellipsometry (M-2000D, J. A. Woollam Inc.) and modeled in CompleateEase software. The bandpass filter designs of 5-layer, 7-layer, and 9-layer stacks were simulated in OpenFilters Software with the materials' modeled refractive indices. Table 1 summarizes the designed layer thicknesses of 5-, 7-, and 9-layer stacks.

Table 1. Designed thicknesses of multilayers at 3250 nm center wavelength.

Layer Order	5-layers	7-layers	9-layers
1.	254.68	404.67	392.15
2.	516.83	536.32	513.31
3.	57.23	224.46	205.58
4.	211.31	203.02	298.25
5.	192.69	62.28	29.86

6.	354.89	528.34
7.	312.01	313.25
8.		353.63
9.		51.12

The designed 7-layer bandpass filter was deposited on a 0.5 mm thick sapphire substrate in an e-beam evaporation chamber (TORR Evaporation Systems). Table 2 shows the simulated thickness of every layer of the design before fabrication and their measured thickness after fabrication.

Table 2. Simulated and fabricated thickness comparison of layers.

Materials	**Simulated thickness (nm)**	**Measured thickness (nm)**
Ge	404.67	439.85
Al_2O_3	536.32	520.66
Ge	224.46	232.46
Al_2O_3	203.02	211.58
Ge	62.28	60.50
Al_2O_3	354.89	320.67
Ge	312.01	324.29

2.4.2. Preparation of the Pyroelectric Detector

The top and back electrodes of a z-cut $LiTaO_3$ crystal substrate were coated in TORR e-beam evaporation system. Deposition base pressure was set at $4.2x10^{-6}$ mbar for each deposition to obtain equal coating quality. With a 7x7 mm^2 area opening of a shadow mask, the top electrode was made by coating 6 nm thick chromium and gold metals. Then the shadow mask was changed, and 95 nm thick gold was coated to form a contact pad. Then, the sample was turned upside down, and 6 nm chromium followed by 40 nm gold was coated to form the back electrode. After electrode coatings, die bonding was conducted to establish the electrical connection between the detector and measurement instruments. The single element detector needs to be mounted on a PCB board, followed by mounting of the PCB board to the measurement board (Ossila ZIF test board). Finally,

the connection is completed by connecting the measurement board to the measurement system via a BNC cable.

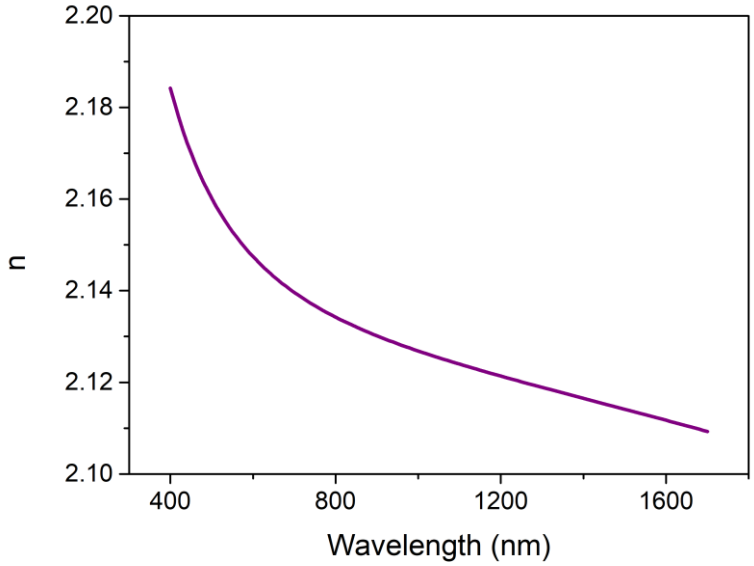

Figure 11. Refractive index versus wavelength graph of $LiTaO_3$ crystal.

The refractive index values of $LiTaO_3$ were determined by using a J.A. Woollam V-Vase ellipsometer and a *CompleteEase* software. The measured response in the ellipsometer was modeled with a Sellmeier equation, and equation coefficients were obtained from equation 14. The corresponding refractive index versus wavelength graph was plotted as shown in Figure 11. The simulated refractive index values match with earlier reported values [79], [80].

$$n = \left[2.398 + \frac{2.113\lambda^2}{\lambda^2 - 0.13323^2} - 0.02606\lambda\right]^{1/2} \qquad (14)$$

2.4.3. Building of Optical Setup

An optical setup was built to measure the concentration of ethanol gas by correlating voltage output. This optical setup consists of a stabilized benchtop IR light source (SLS303, Thorlabs), two converging lenses, a gas cell with an effective optical length of 10 cm, an optical chopper system (MC2000B, Thorlabs), a 7-layers optical bandpass filter, a pyroelectric detector, a lock-in amplifier (SR530, Stanford Research), a multimeter (DAQ6510, Keithley), a canister and a mass flow controller (GMC1200, Atovac). N_2 gas was used as a carrier gas to direct the ethanol vapor into the gas cell with a constant flow.

2.4.4. Characterization Studies

The transmittance spectra were measured with a Fourier transform infrared (FTIR) spectrometer (Shimadzu IRAffinity-1S) from 600 to 4000 cm^{-1}. For the gas phase studies, a 10 cm gas cell (Pike Technologies) equipped with potassium bromide (KBr) windows was placed inside the sample holder of the FTIR. Ethanol vapor was released from the canister and directed to the gas cell with an air pump. The absorption spectrum of the ethanol vapor was recorded with the FTIR from 600 – 4000 cm^{-1}. By placing the bandpass filter in the path of the gas cell, the transmittance spectrum of the bandpass filter in combination with the ethanol vapor absorption was recorded. Ellipsometric data were collected for Ge and Al_2O_3 single layers, multilayer bandpass filter, and substrates at 55°, 65° and 75° using a V-Vase J. A. Woollam Co., Inc. spectroscopic ellipsometer.

2.5. Results and Discussion

2.5.1. Single Layer Germanium and Aluminum Oxide Coating Multilayer Optical Band pass Filter

300 nm thick single layer of germanium (Ge) and aluminum oxide (Al_2O_3) coating were coated onto each 300 µm thick double-sided polished silicon substrate separately to determine their optical constants. Figure 12 (A-B) show the modeled refractive indices and extinction coefficients of Ge and Al_2O_3 in the range of 600 – 1700 nm. The refractive indices depicted in Figure 12 (A-B) are compared and found to match previously reported values.[81] With the CompleteEase software (JA Woollam), we use the Cauchy dispersion relation to model the ellipsometry measurement of psi and delta. The refractive index, n of Al_2O_3 at 1.7 µm, is 1.52, while the physical thickness, d, is 303 nm with the mean square error (MSE) of 3.3. For Ge, we use the Cody-Lorentz dispersion functions to obtain the refractive index of 4.2 at 1.7 um, while the physical thickness, d, is 301 nm with an MSE of 5.6. As Ge showed absorbance in a large part of the measured range, the Cody-Lorentz dispersion relation was chosen to model the Ge layer. Previous results showed that the Cody-Lorentz dispersion relation modeled the Ge coating with an improved MSE due to the additional parameters to describe the absorption transition just above the band gap energy of the material [81], [82].

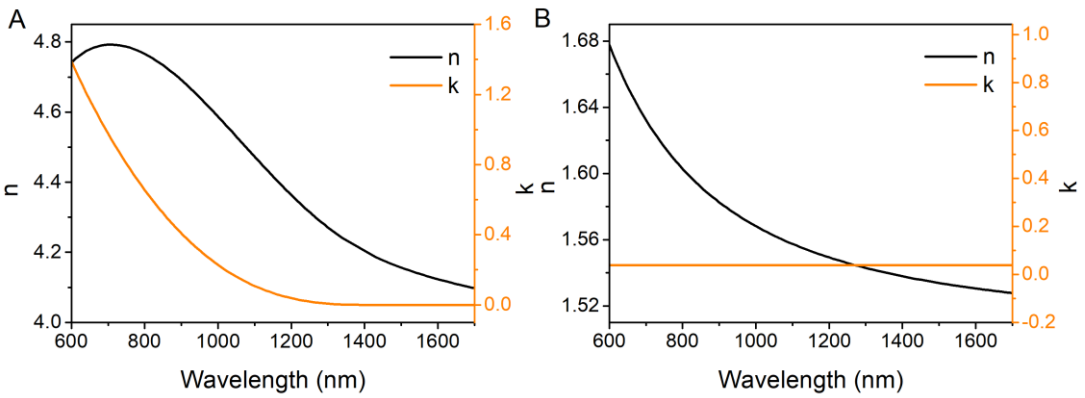

Figure 12. Optical constants of A) thin Ge coating and B) thin Al_2O_3 coating.

Taking into account the absorption range of ethanol at 3.2 µm, which is attributed to the CH stretching of the gas molecule, we designed a multilayer bandpass filter with a maximum peak at 3.2 µm and a bandwidth of 464 nm. Ge and Al_2O_3 are suitable materials for this optical filter as they are transparent in the required mid-infrared spectrum. Ge is the high refractive index material in the design, while Al_2O_3 is the low refractive index material. This pair of materials offers a large diffractive index difference, enabling the filter to achieve high transmittance with fewer layers [64]. As a result, the thermal stress mismatch can be reduced [69]. We evaluated three different bandpass filter designs based on different numbers of layers, including 5, 7, and 9 layers. The design methodology is based on two steps approach. First, two highly reflective Bragg mirrors; a long-wave pass filter and a short-wave pass filter with quarter-wavelength layers are designed separately. The layers of the two mirrors are added up, which optically overlaps at the center passband (3250 nm) with the desired bandwidth (464 nm) [64], [69]. Secondly, the whole stack is optimized with the software's optimization algorithm and with the target set to the desired selected wavelength range [83]. These optimized layers enable incident light interference that reflects constructively or destructively. Thus, allowing a specific range of wavelengths with the desired intensity to transmit. Table 1 shows the thicknesses for the various designs. The simulated transmission profiles of the different designs are shown in Figure 13A. Among the designs, we chose to fabricate the 7 layers bandpass filter for several reasons. The 7-layer design is better than the 5-layer design due to its narrower transmittance bandwidth and higher transmittance intensity. The 9-layer design shows only a slight improvement in the transmittance compared to the 7-layer design. Theoretically, we could design a higher number of layers, but the available coating

process limits the feasibility of coating a higher number of layers due to coating stress and coating exfoliation. Therefore, the 7-layer design is a compromise to achieve the required specification for this work. The construction of the 7-layer band pass filter consists of alternating high and low refractive indices materials. Description (15) shows a representation of the bandpass filter design, where H represents the high refractive index material, L represents the low refractive index material, Air is the medium around the bandpass filter, and Al_2O_3 is the sapphire substrate.

$$Air|Al_2O_3|HLHLHLH|Air \qquad (15)$$

The 7-layer band pass filter was prepared according to the design parameters. Figure 13B shows the measured transmittance profile of the bandpass filter (FTIR measurement) in comparison with the simulated transmittance profile from the design (OpenFilters) and the simulated transmittance profile with inputs from the experimentally measured thickness and optical constants (Ellipsometry model). The bandpass filter has a maximum transmittance of 84.5% centered at 3250 nm and a bandwidth of 464 nm. The measured transmittance profile matches the designed and simulated transmittance profiles reasonably well. The thickness parameter for each layer is extracted from the modeled band pass filter using the described dispersion functions set constant for each material in the 7 layers structure. Then, the thicknesses for each layer and the materials' optical constants are used as inputs to simulate the transmittance spectrum. Since the last values of the measured optical constants at 1700 nm are used to extrapolate into the mid-infrared region in the software, several iterations for the reverse synthesis analysis of the bandpass filter have been performed to obtain a better match. The modeled optical constants (n and k values) for Ge and Al_2O_3, and the thickness of each layer were optimized to obtain the best fit with the measured transmittance spectrum [67]. Analysis shows that the resulting thickness values are slightly different from the designed values (Table 2), with an average deviation of 4.5% for Ge, and 5.5% for Al_2O_3.

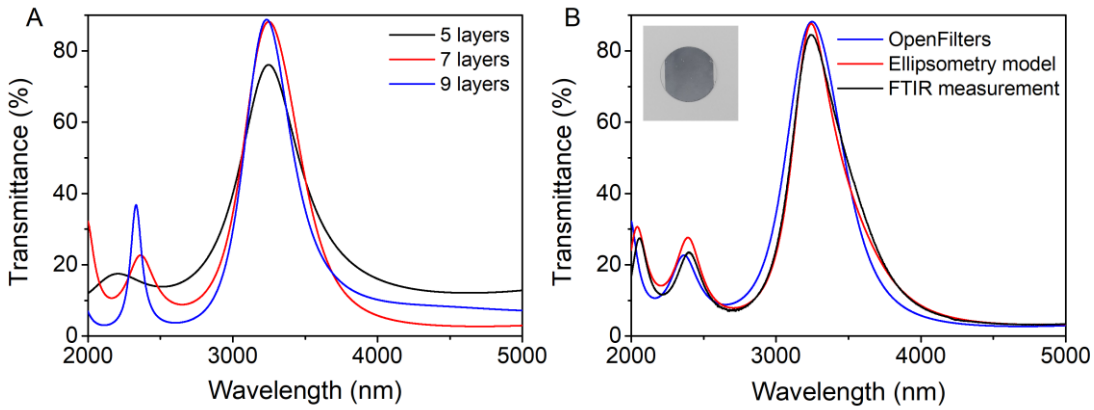

Figure 13. A) Designed transmittance profiles of 5, 7, and 9 layers band pass filters on sapphire substrate B) Transmittance profiles of 7-layer band pass filter. The black spectrum is the measured spectrum. The red spectrum is simulated with the thickness measured on SE. The blue spectrum is designed and simulated using OpenFilters. Inset in the figure shows the image of the fabricated band pass filter.

To verify the multilayer bandpass filter and its purpose in detecting CH stretching of gas molecules, we place the prepared filter in front of a 10 cm gas cell filled with ethanol vapor to perform a gas phase transmittance measurement on an FTIR spectrometer. Figure 14 shows the transmittance measurement of the multilayer bandpass filter in the presence of ethanol vapor. Among the characteristic peaks of ethanol [84], the vapor spectrum shows an absorption peak around 2900 cm^{-1} that can be assigned to the vibrational mode of the CH stretching. The overlap between the bandpass filter's transmittance peak and the absorption peak clearly shows that the bandpass filter can allow selected transmitted light to pass, which corresponds to the ethanol's absorption peak. Thus, enabling the selective detection of ethanol vapor. As a result, a detector placed after the gas cell will detect a signal drop as the infrared light that shines through the gas cell is absorbed by the ethanol vapor. The signal drop is an indication that the detector detects the presence of ethanol vapor.

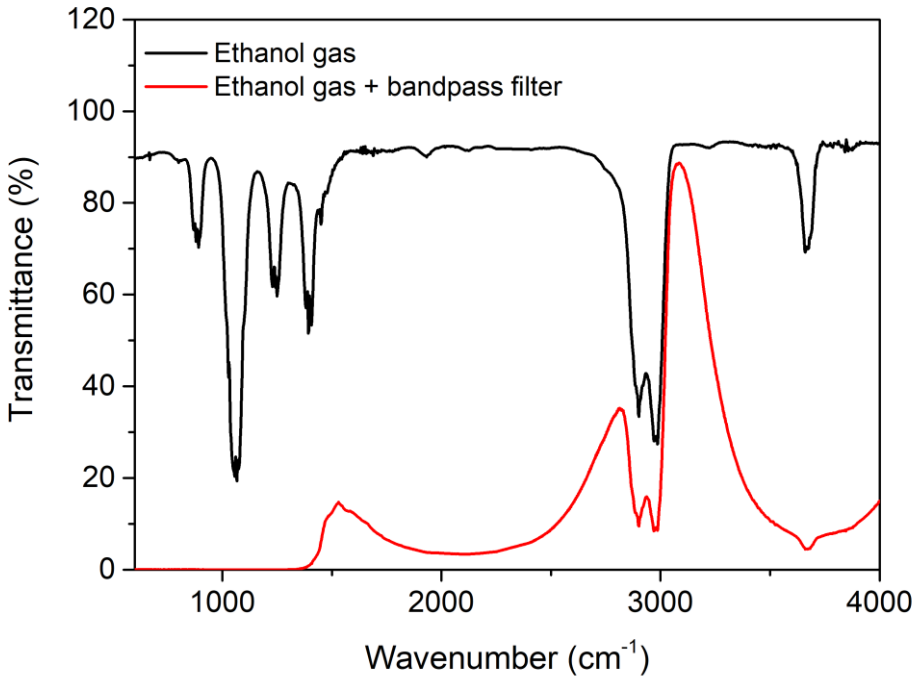

Figure 14. FTIR measurement of ethanol gas (black line) and multilayer band pass filter in the presence of ethanol gas (red line).

2.5.2. Pyroelectric Detector

Figure 15A-B show the schematic of the characterization setup to characterize the detector and the components of the $LiTaO_3$ pyroelectric detector. The fabricated $LiTaO_3$ pyroelectric single element detector consists of a thin z-cut $LiTaO_3$ substrate (60 ± 10 µm), top and bottom electrodes, gold wire bonds, and a printed circuit board for mounting of the device. Then, the mounted device is placed on a test board (Ossila) for electronic characterization. In this work, we investigate the z-cut $LiTaO_3$ in which the polar axis is in perpendicular configuration to the active surface of the substrate. Such cut is an advantage for our pyroelectric application attributed to the convenience of fabricating the pyroelectric device and its electrodes in a layered structure [85]. The top and bottom electrodes can be fabricated easily to collect charge accumulation on opposite surfaces upon temperature change. To determine the ideal working range of the fabricated pyroelectric detector, we build a characterization setup as shown in Figure 15. The characterization setup consists of a broadband infrared light source, an iris to reduce the beam diameter, lenses to focus the light onto the connected pyroelectric detector, an optical chopper to induce temperature change at a specific frequency, a lock-in amplifier, and a multimeter system to amplify and measure the electronic signal of the detector.

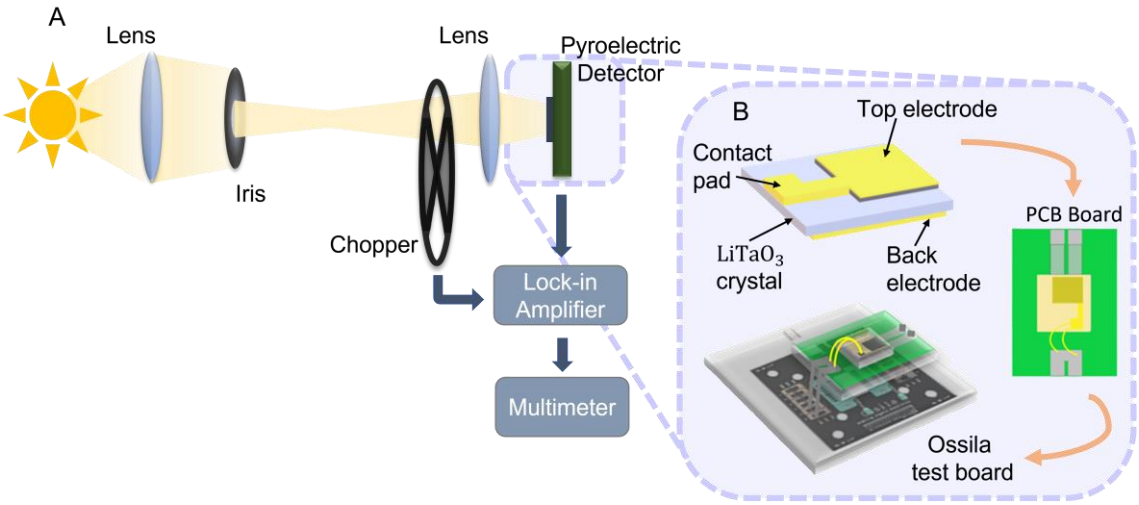

Figure 15. A) Schematic of the detector characterization setup. B) Components of the $LiTaO_3$ pyroelectric detector.

$$R_v = R_i \times \frac{R}{\sqrt{1 + (2\pi f R C)^2}} \quad (16)$$

Figure 16A – 16D show the photoresponse and electronic signals of the $LiTaO_3$ pyroelectric detector as a function of the chopping frequency. Figure 16A represents the detector's voltage response, V_{out}, curves for frequency swept between 4 Hz to 40 Hz. The output voltage of the detector drops from 40.6 mV to 28.2 mV at 7Hz, equivalent to a 70.7% (3 dB) drop from the maximum amplitude. There are several parameters to characterize the performance of a pyroelectric detector, including responsivity voltage (R_v), noise voltage (V_{noise}), noise equivalent power (NEP), specific detectivity, and D-star (D*) [86]. Figure 16B shows the responsivity voltage curves of the pyroelectric detector. The ratio of the output voltage generated V_{out} and the incident radiation power on the detector, P (W), determines the responsivity voltage, R_v of the sensor. With the semi-empirical method, we can estimate the responsivity voltage R_v as a function of frequency using the following equation (Equation 16). The responsivity voltage, R_v can be determined by multiplying the responsivity current, R_i, with the effective impedance (ohm). In the equation, R_i is the responsivity current (A/W), R is the detector's total resistance (ohm), f is the chopping frequency (Hz), and C is the pyroelectric detector's capacitance (farad). The measured capacitance of the detector is 0.595 nF, while the resistance, R, is 250 MΩ. By comparing the curves in Figure 16B, we find that the calculated curve agrees with the measured curve.

$$NEP = \frac{V_{noise}}{Responsivity} \quad (17)$$

According to a previous study, noise can be a problem when detecting a small signal of a pyroelectric detector. To understand the detection limit and sensitivity of the detector, we characterize the noise signal and the output signal to identify the smallest signal that cannot be differentiated from the background noise. Commonly, this is understood as the signal-to-noise ratio of a detector. However, for a $LiTaO_3$ device, the smallest signal that the detector can measure is determined by the noise equivalent power (NEP). Equation 17 shows the relationship of NEP with V_{noise} and R_v. To determine the NEP, we evaluate the voltage noise of the detector without any input power [87]. Figure 16C shows the measured V_{noise} curve at different frequencies and the equivalent noise bandwidth of 1 Hz. This noise signal measurement allows us to determine the frequency dependence of the noise signal contributed typically by two significant sources of noise; thermal noise and Johnson noise [87], [88]. The noise level of the detector is between 2 x 10^{-5} $V/Hz^{1/2}$ to 1.6 x 10^{-4} $V/Hz^{1/2}$. By considering the noise signal and the responsivity voltage, we determine the calculated NEP curve (Figure 16D). With this, we identify that the operating frequencies that provide the best signal-to-noise ratio fall between 4 Hz and 30 Hz. Above these frequency values, the NEP increases, thus affecting the output voltage signal. Despite these operating ranges, the magnitude of the output signal falls off quickly from 7Hz onwards. In such a situation, the user must make a compromise by selecting the operating frequency to achieve the desired voltage magnitude while maintaining a low NEP. In the ethanol detection application, we select a 12 Hz chopping frequency which provides an NEP value of 1.15642E-5 $WHz^{-1/2}$. Since the performance of the pyroelectric detector is area dependent, the detector's performance can be normalized to a constant detector area. This normalization method allows detectors of different sizes to be compared equally. Thus, a parameter known as D* is introduced, which depends on the area of the detector, A_d, and NEP (equation 18). We calculate the D* of the pyroelectric detector to be 60531.64 $cmHz^{1/2}\,W^{-1}$ at a 12 Hz chopping frequency.

$$D^* = \frac{\sqrt{A_d}}{NEP} \quad (18)$$

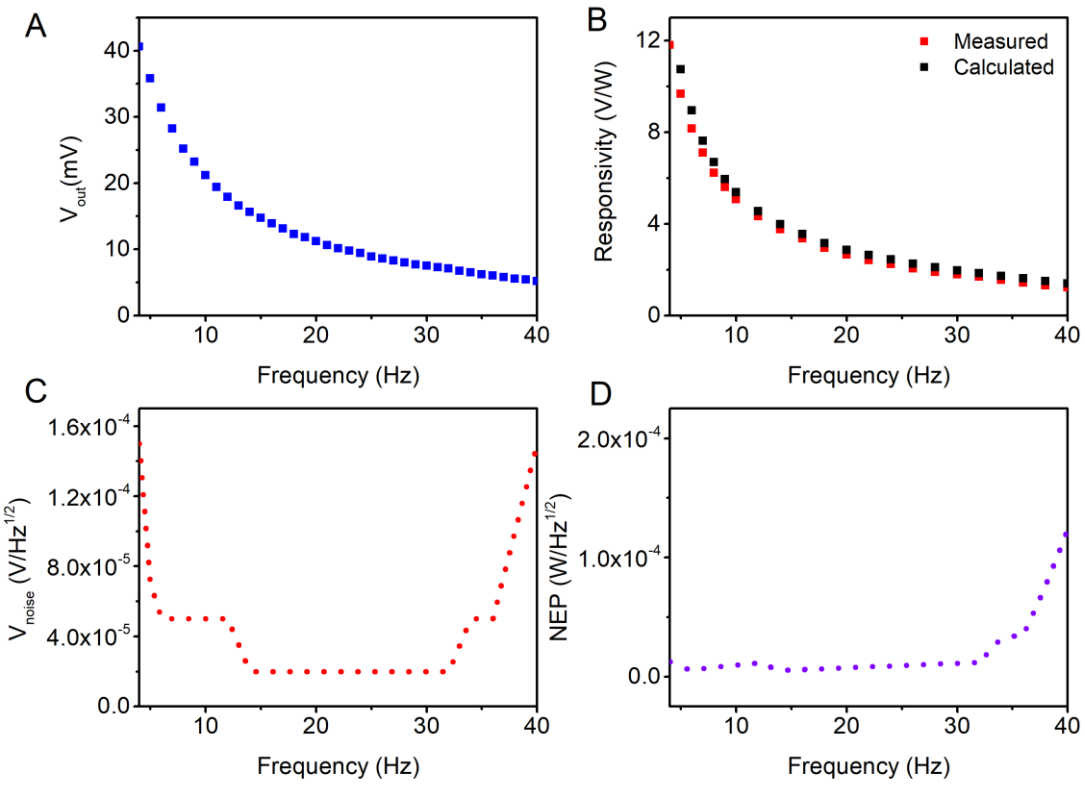

Figure 16. A) Voltage response of the detector as a function of the chopping frequency B) Measured and calculated responsivity voltage. C) V_{noise} measurement with respect to modulation frequency with no power input. D) NEP measurement with respect to modulation frequency with no power input.

2.5.3. Optical Setup Measurements

After fabrication of the band pass filter and the pyroelectric detector, we constructed an NDIR system to investigate the performances of the fabricated components for ethanol concentration sensing. As shown in Figure 17A, the ethanol vapor is carried from the sample compartment with the help of nitrogen gas and is directed into the gas cell with a controlled flow by a mass flow controller. The nitrogen gas acts as a carrier gas for the ethanol vapor to flow into the gas cell. To remove the presence of ethanol in the gas cell, we connect another nitrogen source to flush the gas cell to reset the signal of the pyroelectric detector. Thus, this allows us to perform an experiment showing ethanol's absence and presence in the detection system. The broadband light beam (550 nm to 15 um) is focused with a lens, reduced by an iris, and directed through a 10 cm gas cell with a 20 mm aperture. Then, the light passes through an optical chopper for frequency modulation and a bandpass filter (3250 ± 232 nm). Finally, the beam passes through a lens that focuses the beam onto the pyroelectric detector. This setup is extended to show

that the detection system detects several concentrations of ethanol by volume, including 100%, 75%, 50%, 25%, 12.5%, and 6%. We also show that the detection system can determine the concentration of alcohol in wine and beer, which have 13% and 6% alcohol by volume (ABV), respectively.

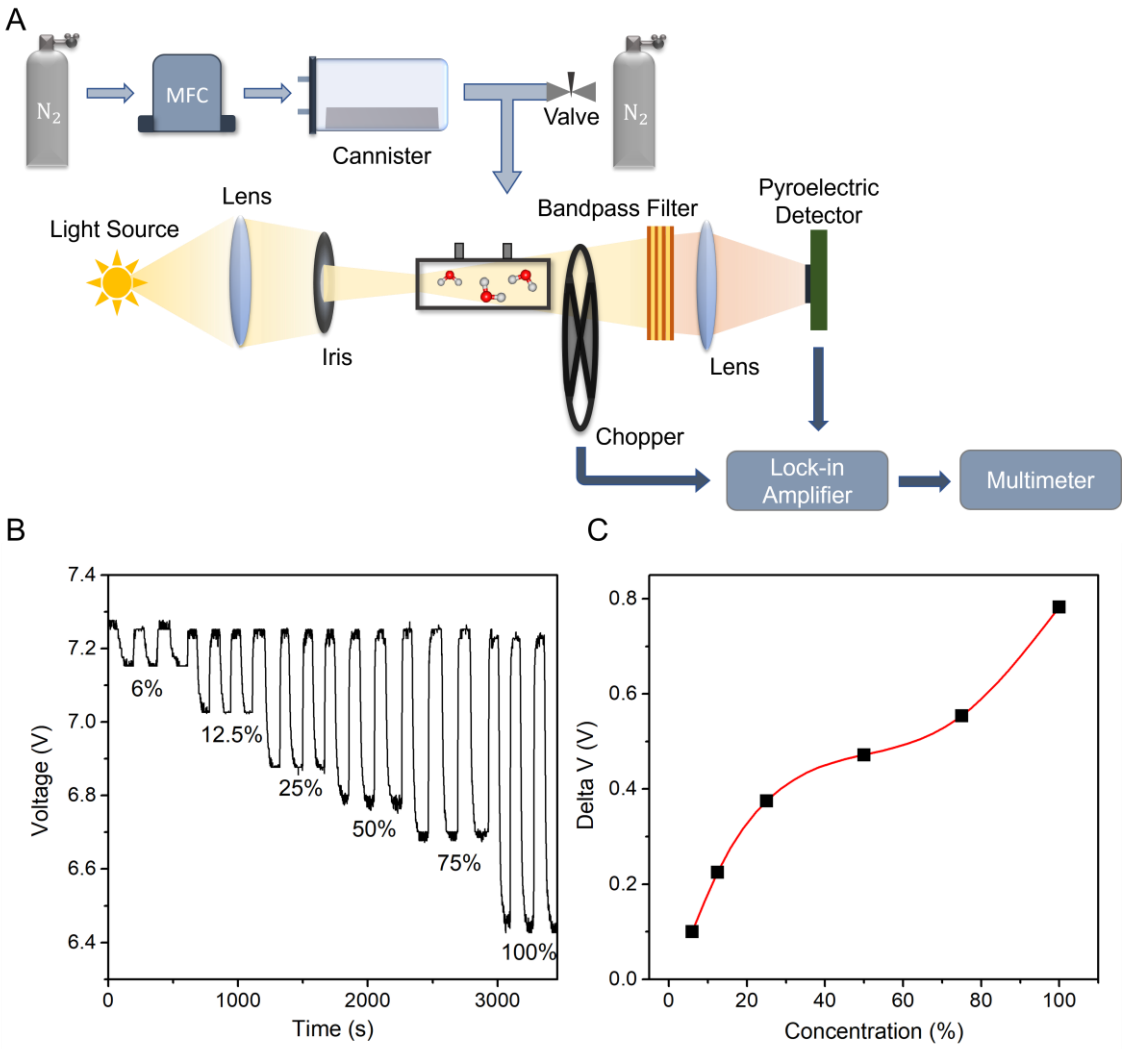

Figure 17. A) Optical setup for gas detection. B) The voltage response of the $LiTaO_3$ pyroelectric detector for different ethanol concentrations by volume. C) The detected voltage difference of each ethanol concentration by volume.

Figure 17B shows the measured voltage response of the pyroelectric detector to detect and quantify ethanol vapor from different ethanol concentrations in the time domain. To achieve higher sensitivity and accuracy in detecting low alcohol concentration, we record the voltage response on the gas detection setup with 10x amplification on the lock-in amplifier. The ethanol vapor is produced in a sample compartment at room temperature of 23°C, and the different concentrations are achieved by preparing ethanol-water

mixtures of different ratios. Since the evaporation and vapor transfer of ethanol are dependent on the horizontal surface area, thus a new absorbing pad of 20 cm x 7 cm dimension is used to hold the 20 ml ethanol-water mixture for each concentration [89]. We supply a constant nitrogen flow of 0.7 SLM into the sample compartment with a mass flow controller and direct the ethanol vapor into the gas cell. Almost instantaneously, the intensity of the detector's voltage response drops sharply, attributed to the absorption of the light source at 3367 – 3449 nm by the ethanol vapor molecules. The specific detection of ethanol is attributed to the 3250 ± 232 nm bandpass filter placed in front of the pyroelectric detector. When the voltage response stabilizes around 100-120 seconds, the ethanol vapor flow is cut off from the gas cell. Then, nitrogen gas is introduced into the gas cell to flush away the remaining ethanol vapor and fill it with nitrogen gas. The detector's voltage response instantaneously rises and returns to the original value of 7.25 V. In this experiment, this step is taken to reset the gas detection system due to the system's specificity to detect only ethanol. After flushing the gas cell with nitrogen for 80-100 seconds and obtaining a stable value of 7.25 V, we repeat the process of introducing the ethanol vapor with nitrogen carrier gas. Then, the experiment for each concentration continues for numerous cycles and ends with ethanol vapor in the gas cell. By merging and comparing the voltage response graphs for each concentration, we show a relationship between the detected voltage response and concentration. As the concentration increases, the voltage response decreases with a larger magnitude. This decreasing trend correlates to the higher amount of ethanol vapor molecules that absorb more light, resulting in a lower voltage value. The ethanol concentrations by volume of 6%, 12.5%, 25%, 50%, 75%, and 100% correspond to the voltage value of 7.16 V, 7.03 V, 6.88 V, 6.79 V, 6.70 V and 6.44 V respectively. With these values, we calculate the difference between the voltage drop and the baseline voltage value of 7.25 V for each concentration. The calculated difference, delta-V, is plotted against the concentration of ethanol in the ethanol-water mixture (Figure 17C). Generally, as the ethanol concentration increases, the delta-V increases. The data clearly shows that the detector can sufficiently distinguish each ethanol concentration. The red line that goes through the data points results from the cubic spline interpolation. The curve line suggests that the voltage response and ethanol concentration relationship is non-linear. This non-linear relationship is manifested by the complex interactions involved in the ethanol-water mixture. In an ethanol-water binary liquid mixture, three types of hydrogen bonding exist attributed to the interactions between ethanol-ethanol, ethanol-water, and water-water

[90]. These interactions affect the evaporation rates of ethanol at the interface, thus resulting in concentration-dependent vapor pressure. The result shown in Figure 18 agrees with previous studies of ethanol vapor in an ethanol-water liquid mixture and indicates the accuracy of the measurement [89]–[91]. The creation of a look-up table from this data set can support the development of a device detecting a wide range of alcohol content in beverages.

As expected, the detection system can detect the concentration of other liquid mixtures, like alcoholic beverages. We show the detection of alcohol concentration of a local beer and a local wine that have their respective alcohol by volume (ABV) concentrations of 5% and 13%. Figures 18A-B show the detector's voltage response in the presence of alcohol vapor generated from beer and wine. The corresponding voltage values are 7.18 V and 7.03 V, respectively. Notably, the detected values are close to the values of 6% and 12.5% ethanol concentration in the ethanol-water liquid mixture, thus, validating the detection system's accuracy in detecting alcohol concentration in beverages. Furthermore, the time to detect the alcohol concentration can be done in under 2 minutes.

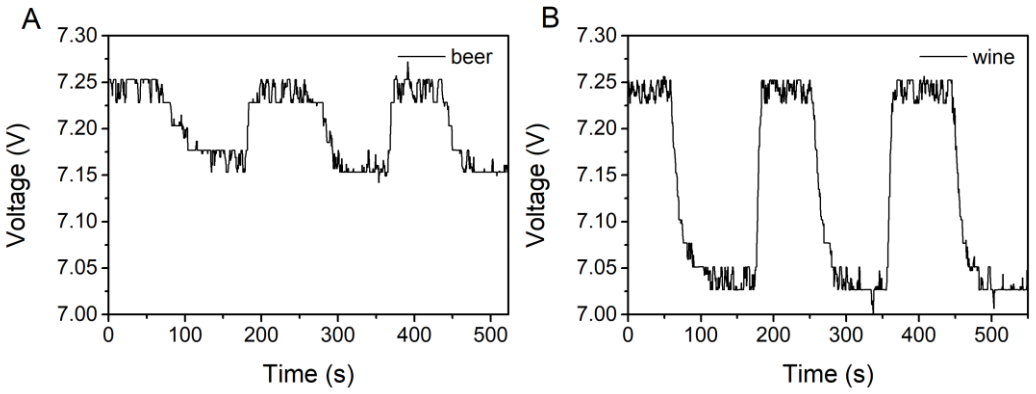

Figure 18. The voltage response of the detector in the detection of beer of 5% ABV (A) and wine of 13% ABV (B).

2.6.Conclusions

In this paper, we show an NDIR gas sensing setup based on a $LiTaO_3$ pyroelectric detector can achieve precise detection of ethanol vapor of different concentrations. We achieved this with the designed 7-layer bandpass filter built with an alternating stack of Ge and Al_2O_3. The maximum transmittance of the optical filter is 84.5%, with the transmittance profile centered at 3250 nm and a bandwidth of 464 nm. The selected wavelength range is well suited for the detection of ethanol attributed to the CH stretching absorption at

3367 – 3449 nm or any other gas molecules which absorb in that range. To complement the gas detection setup, we fabricated a z-cut $LiTaO_3$ pyroelectric detector with the following detector performance. The pyroelectric detector's voltage responsivity is 4.32 V/W, the NEP is 1.16 E-5 W/ $Hz^{1/2}$ and the D* is 60531.64 $cmHz^{1/2}/W$, at 12 Hz chopping frequency. With the right optical bandpass filter (3250 ± 232 nm), optimized chopping frequency, and $LiTaO_3$ pyroelectric detector ($7mm^2$), the detection system can detect the alcohol content of different alcoholic beverages, including beer and wine, in just under 2 minutes. This work suggests that there is potential to extend the capability of such a system to study and detect other gas molecules and the opportunity to miniaturize the detection system with an application-specific integrated circuit to amplify the signal of the pyroelectric detector. However, according to Beer Lambert's law, we recognize that the sensitivity of the optical sensor is dependent and limited by the path length of the gas cell.

The chapter is submitted to the Journal Cell Reports Physical Science.

CHAPTER 3

3. Broadband Light and Heat Management with a Self-Regulating and User-Controlled Thermochromic Smart Window

3.1. Aim of the Study

Space heating and cooling consume half of the total electricity produced globally, and it is a concern for many countries. The energy demand for heating and cooling contributes to rising global emissions. Windows are responsible for huge energy loss primarily by heat exchange between the building's interior and the outside environment. Therefore, scientists have been focusing on developing new thermochromic materials for smart windows to modulate solar irradiation automatically to reduce energy demand for interior comfort. Most of the studies showed visible-light modulation when the temperature rises but lack to show privacy protection during the night when temperature drops. Therefore, this work offers a versatile user-controlled thermoresponsive window integrated with a transparent heater. The sandwiched poly(N-isopropylacrylamide) in a window enables the power-less reversible transition between the transparent and opaque states at its activation temperature. The heater's multilayer coating provides the user with dual functionalities: a privacy switch to darken the window on-demand and an extended spectral reflectivity in the near IR to longwave IR. The vast spectral range helps reduce energy consumption for cooling and heating interior space due to its ability to reflect invisible blackbody radiation. While blocking the heat, the window preserves the transparency for visible light to illuminate the interior.

3.2. Introduction

The world's economic and population growth has led to an increase in energy demand [92]. According to a 2018 study, space heating is responsible for 63.6% of total energy consumption in EU households, whereas space cooling with air conditioners and electric fans is responsible for 20% of the world's total electricity usage today [92], [93]. One of the least energy-efficient components of a building is the window through which energy escape is substantially high [94]. To address this issue, research has progressed towards smart window technologies that focuses on electrochromic [95], [96], photochromic [97], [98], and thermochromic [99]–[101] materials. These different materials allow users to change the window's opacity with applied voltage, light intensity, and temperature. The thermochromic smart window is favorable among the technologies due to its low cost, passive control, and rational temperature regulation [102].

Conventional thermochromic devices are based on a material that undergoes reversible metal-semiconductor transition at a critical temperature. One such material is vanadium dioxide (VO_2), which has a critical temperature of 68°C and a substantial optical contrast in the IR region. Above 68°C, the window changes its state from IR transparent to IR reflective [102], [103]. However, the applied elevated temperature for the transition can undermine the heat-shielding ability of the window. Furthermore, the light transmittance of the window in the transparent state is relatively low at 50 % [104], [105]. As an alternative, thermochromic materials based on hydrogels are employed to regulate transmission in smart window systems [99], [100], [106]–[109]. The recent advancements in thermochromic smart windows rely on functional polymers that can modulate a broad spectrum of light, including ultra-violet, visible, and near-infrared (NIR). The broadband light management by the thermo-responsive polymer embedded in the window enables practical energy-saving purposes associated with cooling and heating indoor space [99], [105]. The emerging interest of developing hydrogel based smart windows led to the development of thermo-responsive hydrogel which include poly(*N*-vinylcaprolactam) [110], thermo-responsive starch [111], hydroxypropyl cellulose [109], [112], [113], polyampholyte hydrogel [114], and poly(*N*-isopropylacrylamide) [99], [100], [115], [116]. Among the thermochromic materials, poly(*N*-isopropylacrylamide) (pNIPAM) has many advantages due to its abrupt response,[115] and reasonable activation temperature.[102], [109] Unlike VO_2 and other thermo-responsive hydrogels, pNIPAM has a lower critical solution temperature (LCST) at 32°C, which works as a practical and

milder activation temperature for a thermochromic window application [99], [100], [117]. Above the LCST, hydrated polymer chains collapse into globules, thus, rendering the polymer insoluble in water [118], [119]. As a result, the window transitions from a transparent state to an opaque state [99], [100]. Despite the vast development of thermoresponsive materials for smart window systems, great opportunities remain in this field, especially in the integrated techniques to improve smart window systems [102]. One of the techniques is the introduction of a transparent heater to enhance the smart widow system from a passive temperature-regulated window to an active-controlled temperature-regulated window. The integrated active control of the thermoresponsive window enables the window to become opaque on-demand, especially at night when the temperature is below the LCST, thus ensuring people's privacy protection.

The development of a transparent heater relies on transparent conductive coating, which is also essential for many applications, including solar cells, light-emitting diodes, touchscreen, car windshield heaters, and heat-responsive windows [120]–[122]. There are many different materials to produce transparent conductive layer, including metal nanofibers [123], metal nanowire mesh [124], metal oxides [121], graphene [125], carbon nanotubes [126], and ultra-thin metal [122], [127]. However, only several materials, including indium tin oxide (ITO) [128], tin wire mesh [113], copper mesh [129], and silver nanowires [111], were used as a transparent heater in electro-thermochromic smart window model.

In this work, we show how ultrathin oxide-metal-oxide (OMO) can be a viable alternative to some of the conductive materials and ITO to obtain an electro-thermochromic smart window integrated with a transparent heater. For the thermochromic function, we use thermoresponsive pNIPAM layer. First, we synthesize pNIPAM and determine its LCST at 32.5 °C with temperature-controlled fluorescence spectroscopy. The temperature at 32.5 °C serves as a practical activation temperature for the window to self-regulate (passive control) its opacity in hot weather. The window can also turn opaque by heat (active control) by applying a low external voltage to the transparent heater. For the transparent heater, we use ultra-thin silver, Ag sandwiched in between two aluminum oxide, Al_2O_3 layers to construct the OMO structure. The advantages of such coating include high visible transparency [130], anticorrosive property [127], thermal stability [131], and spectral uniformity [132]. We use the physical vapor deposition method to fabricate smooth, uniform multilayer (Al_2O_3/Ag/Al_2O_3) coating on a polyethylene

terephthalate (PET) substrate. Before fabrication, we determine the coating thickness based on the design and simulation of the optical transmittance that focuses on balancing the coating's transparency and conductivity. Besides, the materials and thicknesses chosen for the transparent heater extend the window's capability to reflect longwave IR radiation associated with blackbody radiation while retaining the transmittance of visible light. Finally, we merge the transparent heater, 1 mm plexiglass frame, and 2 mm plexiglass to form a thin transparent box. Due to the plexiglass frame, the transparent box has a 1 mm reserved space. To make the smart window model, we inject the pNIPAM solution into the 1 mm space and seal it with waterproof tape. Figure 19 summarizes the operating modes of the proposed smart window model. On a cool day, the window is transparent and allows visible light to illuminate the interior of a building. As the day becomes hotter, at temperatures above the LCST, the thermo-responsive pNIPAM turns into milky latex. The activated pNIPAM enables the opaque state of the window to block the heat induced by solar irradiation in the visible to near IR spectrum. Hence, reducing energy consumption for cooling indoor spaces. Such smart window shows energy-saving capability for buildings in tropical countries and hot summer countries where many rely on air-conditioning to maintain the comfort of the interior [99], [100]. When the temperature drops at night, with the added transparent heater function, users can choose to leave the window transparent or opaque on-demand for privacy. Additionally, while the window allows visible daylight to enter to warm and illuminate the room, it continuously reflects near IR and longwave IR associated with blackbody radiation. The extended spectral capability in the longwave IR is beneficial in reducing energy consumption for cooling and heating interior spaces by blocking excessive thermal heat during hot seasons and maintaining warmth inside the building during cold seasons. Overall, the proposed smart window offers many functionalities, including active and passive heat modulation, visible light regulation, and a "privacy" switch.

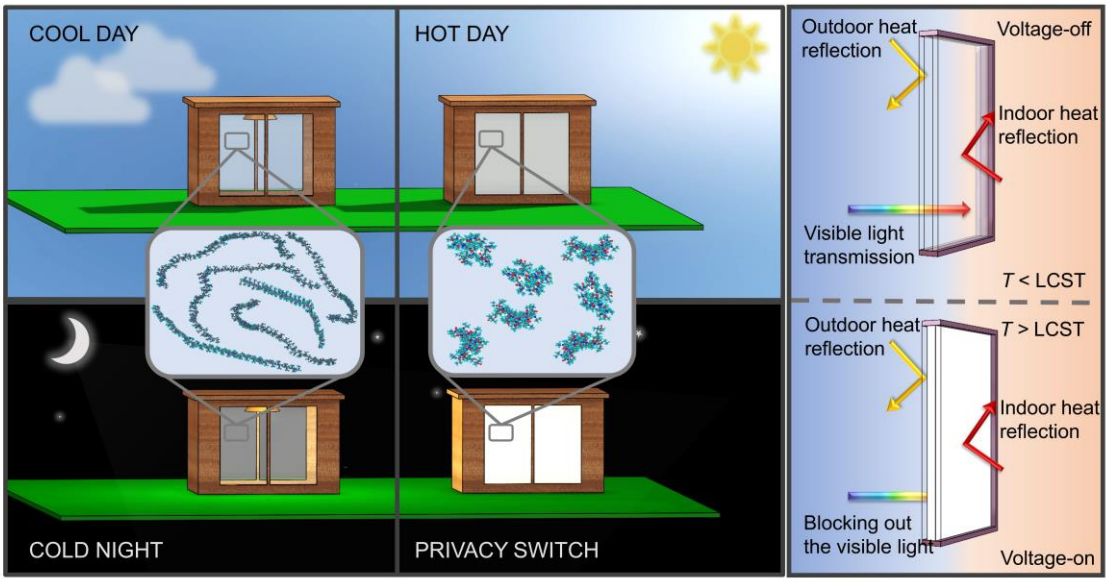

Figure 19. Schematic illustration of the operating modes of smart window throughout the day. The switch between the transparent and opaque states depending on the outdoor temperature and the privacy switch. The image also shows the capability of the window to continuously reflect outdoor heat and indoor heat independent of the LCST.

3.3. Materials

N-isopropylacrylamide (NIPAm, 98%, Sigma-Aldrich), 2,2′-Azobis (2-methylpropionitrile) solution (0.2M in toluene, Sigma-Aldrich), Tetrahydrofuran (THF, Sigma-Aldrich), diethyl ether (Sigma-Aldrich), Rhodamine B powder (Merck kGaA, Darmstadt, Germany), Al2O3 slugs (99.99%, Maideli), Silver (99.9%). All chemicals were used without further purification. DI water was used throughout the experiments. One transparent PET and one 2 mm thick plexiglass of dimensions 10 cm x 10 cm were used.

3.4. Methods

3.4.1. The Synthesis of pNIPAM Homopolymer

The pNIPAM homopolymer was polymerized with the free radical polymerization method using main monomer *N*-isopropylacrylamide (NIPAM) and azoisobutyronitrile (AIBN) as the initiator at 65°C for 8 hours in THF. Firstly, NIPAM (1 g) was dissolved in THF (10mL) in a 2-neck round bottom flask. Then, AIBN solution (0.3 mL) was added dropwise with a syringe. The solution was stirred for 8 hours. Then, the polymer was precipitated in diethyl ether (50 mL) and filtered with Whatman filter paper. The product

was then dried overnight under vacuum at room temperature. ^{1}H NMR (500 MHz, D_2O): δ = 3.9 (1H, s, –NCH–), 2.0–2.2 (1H, –CH–), 1.4–1.8 (2H, –CH_2–), 1.0–1.3 (6H, –CH_3). (Figure 20).

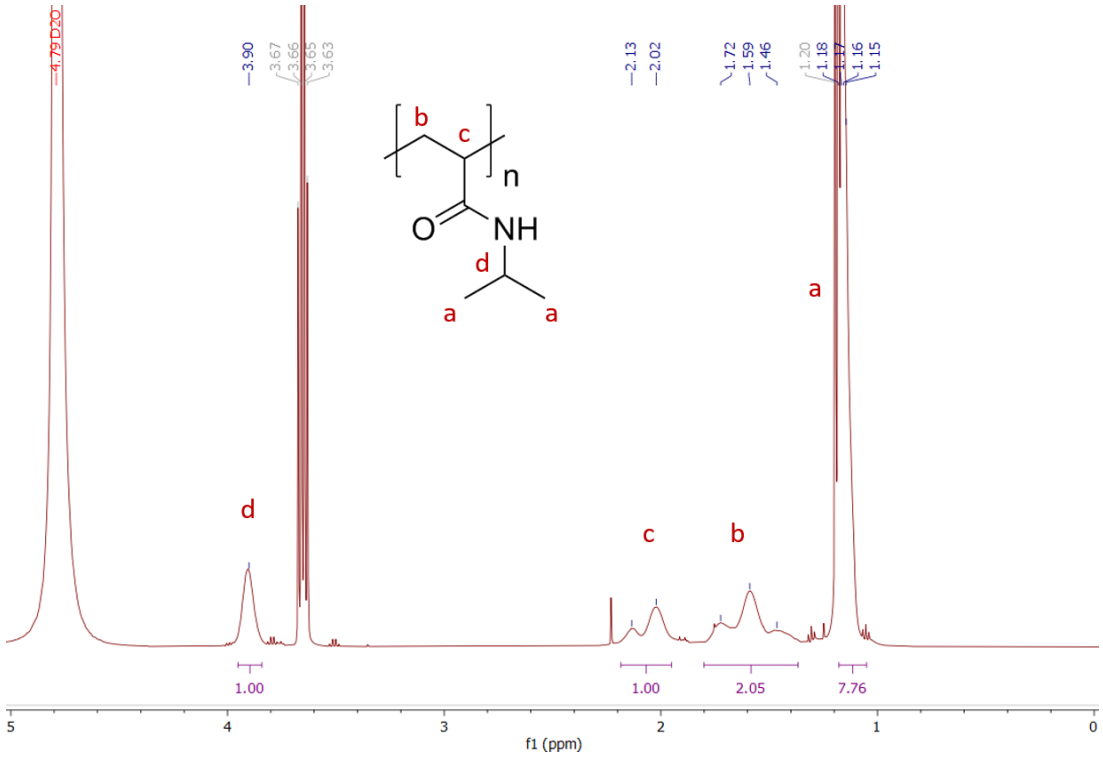

Figure 20. ^{1}H NMR spectrum of pNIPAM.

3.4.2. Heater Design and Fabrication

The layer thicknesses and the transmission profile of ultrathin Ag (UT Ag) -based Al_2O_3/Ag/Al_2O_3 multilayers were simulated by using OpenFilters software. The refractive indexes of substrate and stack materials were measured by spectroscopic ellipsometry (M-2000D, J. A. Woollam Inc.) and modeled in CompleateEase software.

Since the coating is transparent, we model the transparent heater's data using the Cauchy dispersion relation. To achieve an accurate model, we first determine the optical constants of the PET substrate. Then, we model and determine the optical properties of the overall transparent heater‘s structure. Equation 19 shows Cauchy's dispersion equations of the thin Al_2O_3 coating. We obtain the refractive indices of Ag layer using the Lorentz model. Figure 21A and 21B show the refractive indices of the thin Al_2O_3 coating and Ag coating, respectively.

$$n = 1.559 + \frac{0.00044}{\lambda^2} + \frac{0.00003}{\lambda^4} \quad (19)$$

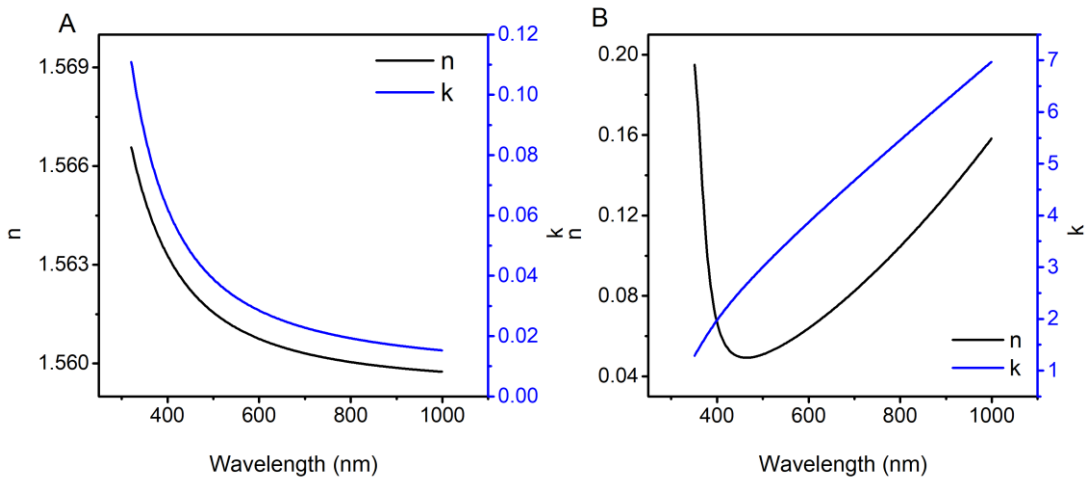

Figure 21. Refractive indices of A) Al_2O_3 B) Ag.

A 0.25 mm thick PET substrate (Hostaphan® GN4600) was cut into 10 cm x 10 cm dimensions and cleaned with soapy water, DI water and Isopropyl alcohol, respectively. It was then dried with nitrogen and placed into the TORR-Evaporator chamber. In the first step, 37 nm Al_2O_3, 12 nm Ag, and 41 nm Al_2O_3 layers were coated respectively, at a 3 x 10^{-6} Torr pressure and 3 Å/s deposition rate with e-beam evaporation technique. Subsequently, the coating was covered with a gap of 0.7 cm on both opposite sides and 130 nm thick Ag electrodes were coated under the same chamber conditions.

Figure 22 shows the schematic of the multilayer coating's cross-section. The transparent heater's coating consists of aluminum oxide, silver, and aluminum oxide (Al_2O_3/Ag/Al_2O_3) stack on a PET substrate. We collect the ellipsometric data in the range between 350 – 1000 nm for the poly(ethylene terephthalate) (PET) substrate and the Al_2O_3/Ag/Al_2O_3 coatings at various incident angles, 55°, 65° and 75°. Then, we model the collected data in CompleteEase software through several iterations of fitting the measured data to a model.

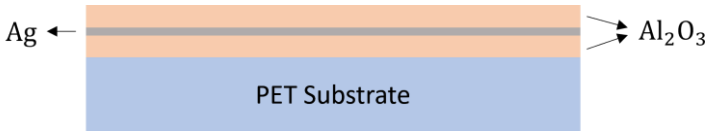

Figure 22. Cross-sectional schematic of OMO stack (Al_2O_3/Ag/Al_2O_3) on PET substrate.

3.4.3. Fabrication of Smart Window

The synthesized pNIPAM (200 mg) was added to DI water (30 mL) and stirred at room temperature until to obtain a homogenous solution. The prepared solution was filtered with a 0.45μm PES filter.

The construction of the smart window is shown in figure 23. A 2 mm thick 10 cm x 10 cm plexiglass, a 1 mm thick 10 cm x 10 cm laser-cut frame, and fabricated heater were sealed together with the help of a transparent aquarium silicone. Then, the sealed window was clamped from the four sides and dried for 24 hours at room temperature. After that, the prepared thermoresponsive polymer solution was injected through a hole into the window and the hole was sealed with waterproof tape.

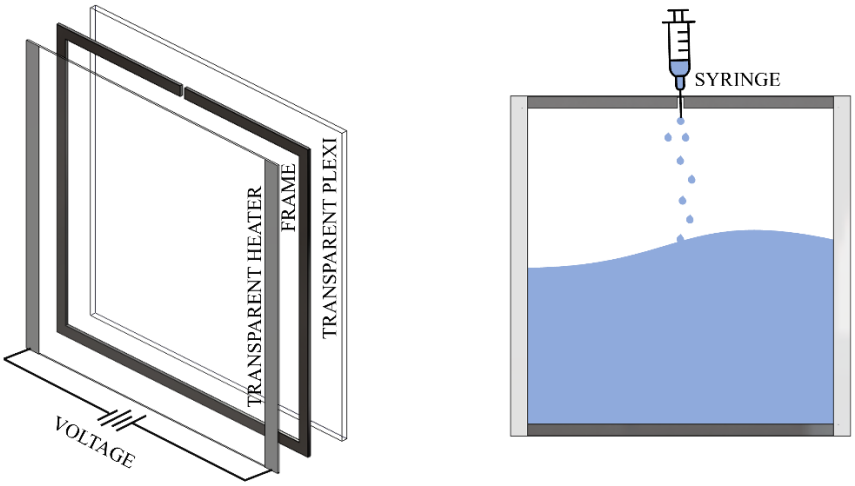

Figure 23. Construction of the heater integrated thermochromic smart window.

3.4.4. Characterization Studies

The transmittance spectra were measured with a UV-vis-NIR spectrometer (Cary 5000, Varian) in the range of 380-2500 nm. ^{1}H nuclear magnetic resonance (NMR) spectroscopy measurements were performed on a Bruker Avance NEO spectrometer (500 MHz) at room temperature. The fluorescence experiments were performed on a fluorescence spectrometer equipped with a temperature controller (Cary, Agilent Technologies). The synthesized pNIPAM (200 mg) was dissolved in DI water (30 mL) and stirred at room temperature. Then, Rhodamine B (0.1 mL, 10^{-4} M) was added into pNIPAM (0.9 mL) solution to track the fluorescence intensity change as the temperature

rises. FTIR spectra were measured with the Fourier transform infrared (FTIR) spectrometer (Shimazdu IRAffinity-1S) from 600 to 4000 cm^{-1}. Sheet resistance of the heater was measured with a four-point probe (C4S57, Cascade Microtech). A programmable DC power supply (UDP1306C, UNI-T) was used to apply an external voltage across the heater. The temperature response of the heater corresponding to the applied external voltage was measured with a K-type thermocouple connected to a multimeter system (DAQ6510, Keithley). Thermal images to show the heat distribution were captured using a compact thermal camera (FLIR Systems).

The T_{lum}, T_{sol}, ΔT_{lum} and ΔT_{sol} were calculated from equation 20 and 21 [133].

$$T_{lum/sol} = \int \Phi_{lum/sol}(\lambda) T(\lambda) d\lambda \Big/ \int \Phi_{lum/sol}(\lambda)\, d\lambda \qquad (20)$$

$T(\lambda)$ indicates the spectral transmittance, $\Phi_{lum}(\lambda)$ is the photopic vision's luminous efficiency function in the wavelength range of 380 –780 nm and $\Phi_{sol}(\lambda)$ is the solar irradiance spectra for air mass 1.5 (corresponding to the sun standing 37° above the horizon with 1.5-atmosphere thickness) between 280-2500 nm. Calculations of integral were applied between the range of 380-780 nm and 280-2500nm for T_{lum} and T_{sol}, respectively.

$$\Delta T_{lum/sol} = T_{lum/sol}(@Temp < LCST) - T_{lum/sol}(@Temp > LCST) \qquad (21)$$

The visible light or solar modulation ability (ΔT_{lum} or ΔT_{sol}) can be determined from the difference in the visible or solar transmittance in the transparent state at low temperatures and opaque state at temperatures above the LCST.

3.5. Results and Discussion

3.5.1. Synthesis of Thermoresponsive Polymer

As the thermoresponsive material, we chose to use pNIPAM homopolymer. We start by synthesizing the pNIPAM homopolymer via free radical polymerization from the monomer *N*-Isopropylacrylamide (NIPAM). Azobisisobutyronitrile (AIBN) is used as the free-radical initiator. We verify the molecular structure of the polymer obtained by performing Fourier transform infrared (FTIR) spectroscopy equipped with the diamond attenuated total reflectance (ATR) accessory in the spectral range of 650-4000 cm^{-1}.

Figure 24A shows the synthetic route of pNIPAM polymerization, and Figure 24B shows the FTIR spectrum of the pNIPAM in solid form. The characteristic pNIPAM peaks at 1540 cm^{-1} and 1645 cm^{-1} are assigned to N-H bending and C=O stretching, respectively [134], [135]. The peaks at 2970 cm^{-1} and 2872 cm^{-1} correspond to C-H asymmetric stretching and C-H symmetric stretching of methyl groups.[136] Furthermore, we assign the bands at 1460 cm^{-1}, 1386 cm^{-1}, and 1364 cm^{-1} to the C-H bending vibrations of isopropyl groups [136], [137]. The band at 3290 cm^{-1} is assigned to the N-H stretching [138].

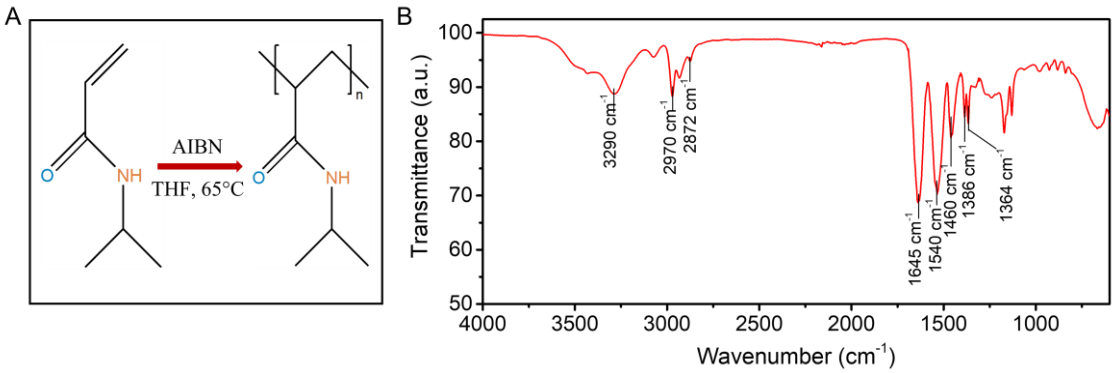

Figure 24. A) Synthetic route of pNIPAM polymerization B) The FTIR spectrum of pNIPAM homopolymer.

The pNIPAM has a unique coil-to-globule transition at its lower critical solution temperature (LCST) around 31 - 33 °C. At this temperature, the soluble polymer chains dehydrate and agglomerate into the insoluble state. Above the LCST, the pNIPAM solution turns from transparent into opaque [136], [139]. We utilize this passive modulating property to block visible light and excessive heat in a smart window configuration. We perform a temperature-controlled fluorescence measurement to determine the LCST of pNIPAM. Since pNIPAM is not an emissive polymer, we mix the fluorescence dye, Rhodamine B, with pNIPAM solution to indirectly obtain the LCST of pNIPAM, which quenches the fluorescence intensity of Rhodamine B as it transitions into the opaque state.

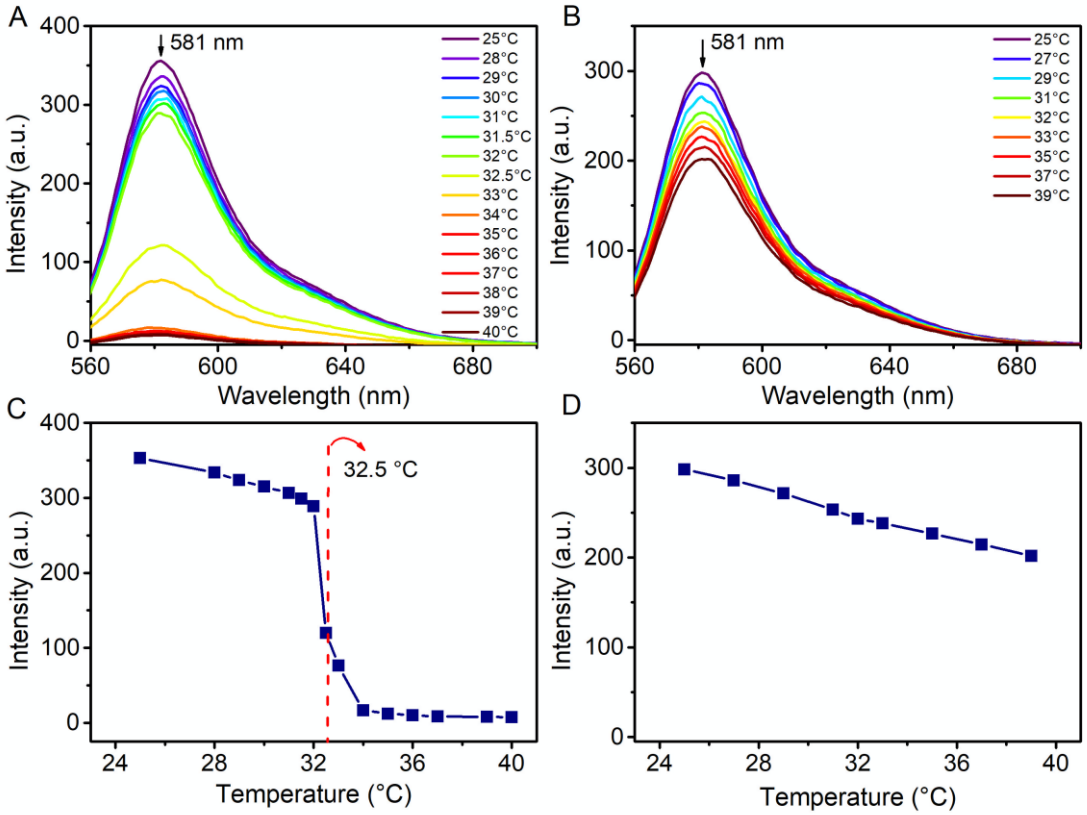

Figure 25. A) Fluorescence spectra of pNIPAM-Rhodamine B solution B) Rhodamine B solution recorded at temperatures between 25-40°C. C) Fluorescence intensities of pNIPAM-Rhodamine B solution D) Rhodamine B solution obtained at 581 nm at corresponding temperatures.

We record the fluorescence spectra of Rhodamine B as we increase the temperature of the pNIPAM-Rhodamine B solution from 25 to 40 °C (Figure 25A). The characteristic emission band of Rhodamine B at 581 nm gradually drops as the temperature increases from 25 to 40 °C. An imminent, sharp decrease in fluorescence intensity is obtained between 32 °C and 33 °C, followed by a total quenching of the fluorescence intensity above 34 °C. To verify whether the sudden drop in fluorescence intensity of Rhodamine B is caused by pNIPAM, not by the temperature response of Rhodamine B,[140] we perform a temperature-controlled fluorescence measurement of Rhodamine B without the presence of pNIPAM. The fluorescence intensity of Rhodamine B at 581 nm decreases gradually with no sign of sudden drop or total quenching at temperatures between 25 to 39 °C (Figure 25B). We conclude that the sudden drop in fluorescence intensity observed in Figure 3A must originate from pNIPAM due to its phase transition at LCST that yields a milky latex solution. The fluorescence intensity of pNIPAM-Rhodamine B solution

recorded at 581 nm is plotted against temperature to determine the exact LCST of the pNIPAM (Figure 25C). In comparison, the plot of the fluorescence peak intensity of Rhodamine B against temperature shows no sudden drop in intensity (Figure 25D). Therefore, we attribute the sharp drop at 32.5 °C to the LCST of the pNIPAM.

3.5.2. Fabrication and Characterization of Transparent Heater

We design and fabricate a multilayer transparent heater to add a heating function to the window. We use aluminum oxide, Al_2O_3, and silver, Ag, as the conductive material. The multilayer transparent heater consists of 3 layers. We coat the 3 layers sequentially on a flexible 250 µm polyethylene terephthalate (PET) substrate using the e-beam evaporation technique. The coating is a stack of $Al_2O_3/Ag/Al_2O_3$ layers. Then, we make voltage busbars on two sides of the coating for voltage application across the heater. This multilayer transparent heater generates heat by inducing a current between the two aluminum oxide layers via the silver layer [130]. The thickness of the silver layer is critical to achieve the required transparency and resistance for the heating effect. Hence, we design the thickness of the $Al_2O_3/Ag/Al_2O_3$ layers to be 37nm/12nm/41nm, respectively. After deposition of the materials, we determine the thicknesses of each layer with an ellipsometer, and we model their refractive indices with the Cauchy dispersion relation and Lorentz model. Next, we use a four-point probe method to measure the sheet resistance, R_{sh} (in Ω sq^{-1}) of the coating. The sheet resistance is typically used to characterize the electrical property of thin coating material, and we find that the fabricated transparent heater has a sheet resistance of 9.5 Ω sq^{-1}. Temperature measurement of the transparent heater is performed by placing a K-type thermocouple on the heater. We measure the heat produced from the heater as we apply various DC voltage values (4.0 V, 6.0 V, 7.9 V, and 8.6 V) across the transparent heater. The voltage applied induces current to flow through the conductive layer, thus resulting in a planar resistive Joule heating. The heat generated for a given area is proportional to the relationship $P = IV$, where P, I, and V are power, current, and voltage. Since the heat produced is directly related to the power dissipated from the transparent heater, we plot the temperature evolution profile of the heater at different input power (1.2 W, 3.0 W, 5.1 W, and 6.0 W) in time (Figure 26A). For every applied power, the temperature increases gradually from room temperature, 21 °C, to a steady-state temperature at which the heater is in thermal equilibrium with the surrounding. It is important to note that for this work, 3 watts of power is sufficient to reach 32 °C, and the transparent heater can reach higher

temperatures by increasing the input power (Inset of Figure 26A). The current-voltage relation in Figure 26B shows a slight deviation from linearity at higher temperatures due to the increased resistivity attributed to the phonon scattering [130], [141]. While achieving a good heating capability, the transparency of the heater is equally important. Hence, we measure the optical transmittance of the transparent heater with a UV-vis spectrometer in the range of 380 – 700 nm. Figure 26C shows the transmittance of PET substrate is 82.4%, and the multilayer coated transparent heater on the PET substrate is 71.5% at 450 nm. As a result, the relative transmittance is 86.7%. The three-layer coating contributes to at least a 10% loss in transmittance due to the reflectance of the coating. To simulate the transmittance of the coating and substrate, we utilized the refractive indices of the materials obtained (Figure 21). The recorded optical properties of the materials enable us to design and optimize coatings in the future. Besides, it can expedite the design process and allow us to simulate the transmittance of the multilayer coating prior to the fabrication process. Figure 26C shows that the simulated spectra fit well with the measured spectra. A good homogenous heater requires a homogenous temperature distribution. For this purpose, we use the IR imaging technique to investigate the heating homogeneity, which facilitates the detection of invisible coating defects. Figure 26D shows the thermal image of the transparent heater, which has a uniform distribution of heat across the surface of the transparent heater. Next, we will show that the transparent heater is an important component for the proposed thermochromic smart window. The advantage of using the $Al_2O_3/Ag/Al_2O_3$ transparent heater in the window configuration is its dual functionalities; as a heater activating the heat-sensitive pNIPAM on-demand and as a reflective coating blocking the heat generated by reflecting the invisible longwave IR spectrum.

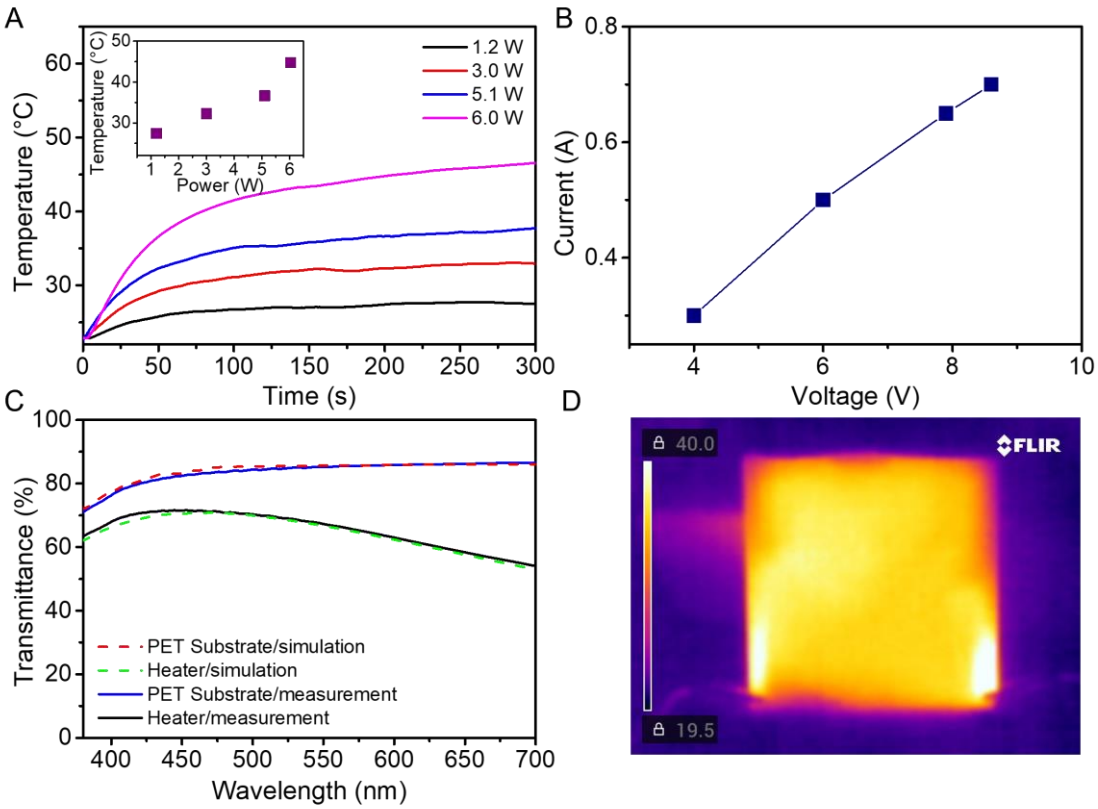

Figure 26. Electrical and optical properties of transparent heater. A) Temperature evolution of the transparent heater at different applied power. Inset shows the temperature measurement taken at 150 s for various input power. B) The current and voltage relationship of the transparent heater. C) Simulated and measured transmittance spectra of PET substrate and the transparent heater. D) IR thermal image of the transparent heater under applied voltage.

3.5.3. Broadband Light Management and Visible Light Modulation of Smart Window

To demonstrate the benefits of the transparent heater to complement pNIPAM, we combine the thermoresponsive pNIPAM solution and the $Al_2O_3/Ag/Al_2O_3$ multilayer stack transparent heater to construct a smart window. We build a smart window model made of a 10 cm x 10 cm plexiglass, a 10 cm x 10 cm laser-cut window frame, and a 10 cm x 10 cm transparent heater. We seal these components together with transparent silicone. Then, we inject the pNIPAM solution into the 1 mm reserved space of the window via a small hole, which is later sealed with waterproof tape. The concentration of the pNIPAM affects the opacity of the windows [116]. Therefore, we ensure to obtain the largest optical contrast by using 6.67 mg mL^{-1} pNIPAM concentration. To demonstrate the temperature response of the window, we imitate the rise in temperature during a hot summer day by conducting an on-off experiment where we apply a bias

voltage of 8.6 V across the heater to heat the window to 40 °C. Figure 27A shows the temperature of the window reaches 40 °C in 650 seconds. As the temperature reaches the LCST of pNIPAM at 32.5 °C, the window becomes translucent (Figure 27B). Above LCST, the window transitions to the opaque state. Once the voltage is turned off, the window cools down gradually. In the cooling process, we see the window's opacity clears up below the LCST, and the window recovers its transparency. Thus, we show a visually distinct reversible transition from the transparent state to the opaque state with high optical contrast regulated by temperature in this window.

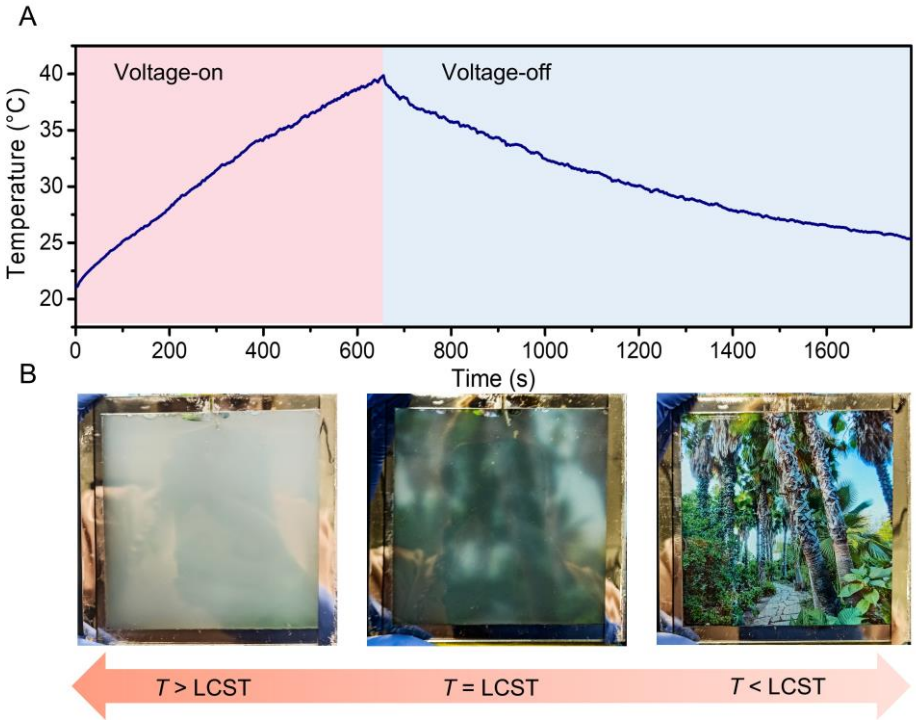

Figure 27. Time-dependent temperature response of the window heated by its transparent heater in an on-off experiment. B) Images of the smart window transitioning between transparent and opaque states due to temperature change that activates/deactivates the sandwiched thermoresponsive pNIPAM layer.

To quantify the optical transmittance of the window when the temperature is below and above the LCST, we measure the vis-NIR transmittance spectra (380 – 2500 nm) of the window (Figure 28A). Below the LCST, the window is transparent, and it shows the highest transmittance of 68.9 % at 450 nm. By increasing the temperature to above LCST, the transmittance drops to 0.4 % at 450 nm. The window shows a very high optical contrast in the visible range. To display the extended optical properties of the window from 2500 nm to 25000 nm, we perform measurements with FTIR spectrometer. Figure

28B shows the window's measured transmittance spectrum (line), calculated reflectance spectrum (dash line), and calculated absorbance spectrum (dotted line) in a comprehensive range between 380 – 25000 nm, obtained by combining NIR and IR measurement results. The results show that the window can manage thermal heat in a broad spectrum by combining the thermoresponsive pNIPAM and the heat reflective coating. The window reflects more than 95% of the long infrared wavelength, which is beneficial during hot seasons as it blocks the invisible heat radiation from entering the cool interior of the building. In cold seasons, the window's coating keeps the building warm by reflecting the radiant heat generated inside the building. The window shows that it has the filtering capability to only reflect the excessive heat energy in the longwave IR without losing visible light transmission. Additionally, the transparent heater in a window provides the user a "privacy" switch to modulate the window's opacity at night when the temperature drops by activating the thermoresponsive pNIPAM layer with heat.

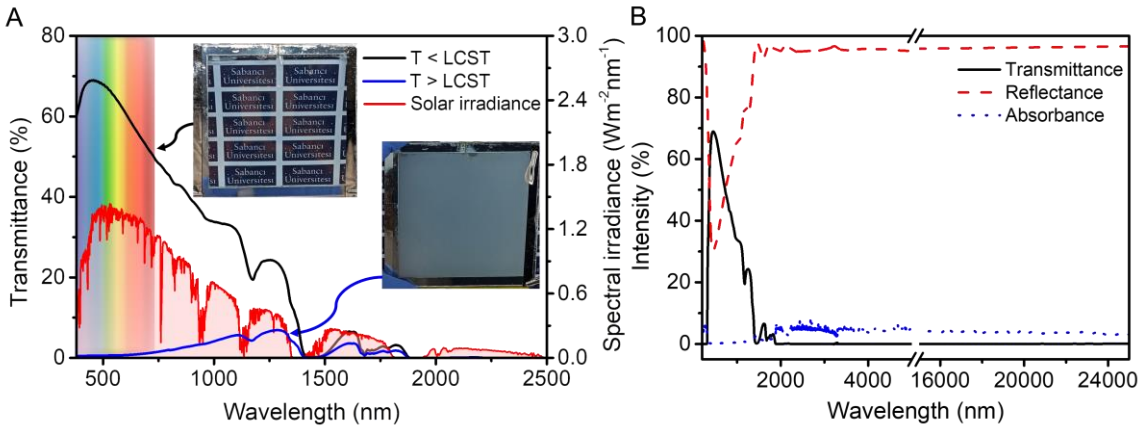

Figure 28. Transmittance spectra of the window recorded at a temperature below and above the LCST. The shaded graph in red represents the solar radiation spectrum [142]. The rainbow color represents the visible range, and the inset shows the images of the window in the transparent state and opaque state (A); the window's measured transmittance spectrum (line), calculated reflectance (dash) and absorbance spectrum (dotted line) in a comprehensive range between 380 – 25000 nm (B).

To quantify the performance of the smart window, we calculate the luminous transmittance and solar modulation ability. At temperatures below the LCST, we calculate the integrated luminous transmittance T_{lum} as 63.9%, and solar transmittance T_{sol} as 45.7%. We quantify the modulation ability of the smart window from the difference of the luminous/solar transmittances $\Delta T_{lum/sol}$, between the transparent state and opaque state. The ΔT_{lum} and ΔT_{sol} are 63.3% and 43.9%, respectively.

3.6.Conclusions

We combine the pNIPAM solution, transparent heater, and low emissive coating to engineer a smart window. We demonstrate how we utilize a thermoresponsive polymer, pNIPAM, in a window to show a window's excellent visible light modulation ability, either in the transparent state (transmittance = 68.9% at 450 nm) or in the opaque state (transmittance = 0.4% at 450 nm). In the transparent state, higher transmittance can be achieved if a substrate with better transmittance such as glass is used. The LCST of pNIPAM at 32.5 °C can be reached quickly with the integrated transparent heater to obtain the opaque state, thus granting the user a "privacy" switch. At temperatures below LCST, we report T_{lum} as 63.9% and T_{sol} as 45.7%. With the phase transition, above LCST, the smart window's visible and solar modulation ability, ΔT_{lum} and ΔT_{sol} are determined as 63.3% and 43.9%, respectively. Moreover, the coating of the transparent heater can block most of the broadband IR heat radiation (Reflectance > 95%, between 2000 – 25000 nm) in the transparent state without affecting the visible light transmitting through the window. This active and passive modulation ability of smart window is useful in buildings where users require energy-saving functionalities for hot and cold seasons and privacy protection at night when the temperature drops. The silver-based oxide-metal-oxide transparent heater with a sheet resistance of 9.5 Ω sq^{-1} shows its potential as a transparent heater for smart window application (relative transmittance = 86.7% at 450 nm).

REFERENCES

[1] L. Liu *et al.*, "Robust and durable surperhydrophobic F-DLC coating for anti-icing in aircrafts engineering," *Surface and Coatings Technology*, vol. 404, p. 126468, Dec. 2020, doi: 10.1016/J.SURFCOAT.2020.126468.

[2] H. Liu, S. Jiang, X. Zhao, H. Jiang, and W. Zhang, "YSZ/Al2O3 multilayered film as insulating layer for high temperature thin film strain gauge prepared on Ni-based superalloy," *Sensors and Actuators A: Physical*, vol. 279, pp. 272–277, Aug. 2018, doi: 10.1016/J.SNA.2018.06.032.

[3] Q. Yang, L. R. Zhao, and P. Patnaik, "Erosion performance, corrosion characteristics and hydrophobicity of nanolayered and multilayered metal nitride coatings," *Surface and Coatings Technology*, vol. 375, pp. 763–772, Oct. 2019, doi: 10.1016/J.SURFCOAT.2019.07.074.

[4] P. K. Kannan, R. Saraswathi, and J. B. B. Rayappan, "CO2 gas sensing properties of DC reactive magnetron sputtered ZnO thin film," *Ceramics International*, vol. 40, no. 8, pp. 13115–13122, Sep. 2014, doi: 10.1016/J.CERAMINT.2014.05.011.

[5] M. L. Addonizio, M. Ferrara, A. Castaldo, and A. Antonaia, "Air-stable low-emissive AlN-Ag based coatings for energy-efficient retrofitting of existing windows," *Energy and Buildings*, vol. 250, p. 111259, Nov. 2021, doi: 10.1016/J.ENBUILD.2021.111259.

[6] B. Baloukas, S. Loquai, and L. Martinu, "VO2-based thermally active low emissivity coatings," *Solar Energy Materials and Solar Cells*, vol. 183, pp. 25–33, Aug. 2018, doi: 10.1016/J.SOLMAT.2018.03.048.

[7] X. Wang, T. Luo, Q. Li, X. Cheng, and K. Li, "High performance aperiodic metal-dielectric multilayer stacks for solar energy thermal conversion," *Solar Energy Materials and Solar Cells*, vol. 191, pp. 372–380, Mar. 2019, doi: 10.1016/J.SOLMAT.2018.12.006.

[8] E. T. Hu *et al.*, "Multilayered metal-dielectric film structure for highly efficient solar selective absorption," *Materials Research Express*, vol. 5, no. 6, p. 066428, Jun. 2018, doi: 10.1088/2053-1591/AACDB3.

[9] D. Kim *et al.*, "Ti/TiO2/SiO2 multilayer thin films with enhanced spectral selectivity for optical narrow bandpass filters," *Scientific Reports*, vol. 12, no. 1, p. 32, Dec. 2022, doi: 10.1038/s41598-021-03935-z.

[10] C. D. Appleget, A. M. Hodge, A. M. Hodge, and C. D. Appleget, "Optical and Mechanical Characterization of Sputtered AlN/Ag Multilayer Films," *Adv. Eng. Mater*, vol. 21, p. 1801268, 2019, doi: 10.1002/adem.201801268.

[11] K. Ratra, M. Singh, A. K. Goyal, and R. Kaushik, "Design and Analysis of Broadband Reflector for Passive Radiative Cooling," in *2019 International Conference on Signal Processing and Communication, ICSC 2019*, 2019, pp. 300–303. doi: 10.1109/ICSC45622.2019.8938212.

[12] A. Jiménez-Solano *et al.*, "Aperiodic Metal-Dielectric Multilayers as Highly Efficient Sunlight Reflectors," *Advanced Optical Materials*, vol. 5, no. 9, p. 1600833, May 2017, doi: 10.1002/adom.201600833.

[13] K. T. Lee, S. Y. Han, Z. Li, H. W. Baac, and H. J. Park, "Flexible High-Color-Purity Structural Color Filters Based on a Higher-Order Optical Resonance Suppression," *Scientific Reports 2019 9:1*, vol. 9, no. 1, pp. 1–8, Oct. 2019, doi: 10.1038/s41598-019-51165-1.

[14] C. Yang *et al.*, "Compact Multilayer Film Structure for Angle Insensitive Color Filtering," *Scientific Reports 2015 5:1*, vol. 5, no. 1, pp. 1–5, Mar. 2015, doi: 10.1038/srep09285.

[15] M. A. Butt, S. A. Fomchenkov, and S. N. Khonina, "Multilayer dielectric stack Notch filter for 450-700 nm wavelength spectrum," in *CEUR Workshop Proceedings*, 2017, vol. 1900, pp. 1–4. doi: 10.18287/1613-0073-2017-1900-1-4.

[16] P. Rouquette, P. Rouquette, C. Amra, M. Zerrad, and M. Lequime, "Micro-cavity optimization for ultra-sensitive all-dielectric optical sensors," *Optics Express, Vol. 30, Issue 9, pp. 15344-15364*, vol. 30, no. 9, pp. 15344–15364, Apr. 2022, doi: 10.1364/OE.457061.

[17] H. Tang *et al.*, "Multichannel Bandpass Filters for Reconstructed High-resolution Spectral Imaging in Near-infrared Fundus Camera," *Sensors and Materials*, vol. 34, no. 4, pp. 1601–1615, 2022, doi: 10.18494/SAM3759.

[18] L. Fleming, D. Gibson, S. Song, C. Li, and S. Reid, "Reducing N2O induced cross-talk in a NDIR CO2 gas sensor for breath analysis using multilayer thin film optical interference coatings," *Surface and Coatings Technology*, vol. 336, no. August 2017, pp. 9–16, 2018, doi: 10.1016/j.surfcoat.2017.09.033.

[19] E. Hecht, *Optics*, 5th ed. Pearson Education, 2017.

[20] B. McDermott *et al.*, "The Fresnel Coefficient of Thin Film Multilayer Using Transfer Matrix Method TMM," *IOP Conference Series: Materials Science and Engineering*, vol. 518, no. 3, p. 032026, May 2019, doi: 10.1088/1757-899X/518/3/032026.

[21] F. L. Pedrotti, L. M. Pedrotti, and L. S. Pedrotti, "Interference of Light," in *Introduction to Optics*, Cambridge University Press, 2019, pp. 163–191. doi: 10.1017/9781108552493.010.

[22] T. R. Matin, M. K. Leong, B. Y. Majlis, and I. C. Gebeshuber, "Correlating Nanostructures with Function: Structural Colors on the Wings of a Malaysian Bee," *AIP Conference Proceedings*, vol. 1284, no. 1, p. 5, Oct. 2010, doi: 10.1063/1.3515563.

[23] H. A. Macleod, *Thin-Film Optical Filters*. 1986. doi: 10.1887/0750306882.

[24] S. Larouche and L. Martinu, "OpenFilters: Open-source software for the design, optimization, and synthesis of optical filters," *Applied Optics*, vol. 47, no. 13, 2008, doi: 10.1364/AO.47.00C219.

[25] S. J. Orfanidis and T. Monica, “Electromagnetic Waves and Antennas,” 1999, Accessed: Jun. 15, 2022. [Online]. Available: www.ece.rutgers.edu/~orfanidi/ewa

[26] J. F. Mohammad, F. H. Antar, and S. M. Abed, “Ultra-narrow Bandpass interference filter for infrared application,” *International Journal of Emerging Trends & Technology in Computer Science (IJETTCS)*, vol. 5, no. 2, pp. 129–132, 2016, Accessed: Aug. 05, 2021. [Online]. Available: www.ijettcs.org

[27] A. Yenisoy, C. Yesilyaprak, K. Ruzgar, and S. Tuzemen, “Ultra-broad band antireflection coating at mid wave infrared for high efficient germanium optics,” *Optical Materials Express*, vol. 9, no. 7, p. 3123, Jul. 2019, doi: 10.1364/OME.9.003123.

[28] J. Yun, “Ultrathin Metal films for Transparent Electrodes of Flexible Optoelectronic Devices,” *Advanced Functional Materials*, vol. 27, no. 18, May 2017, doi: 10.1002/ADFM.201606641.

[29] O. O. Abegunde, E. T. Akinlabi, O. P. Oladijo, S. Akinlabi, and A. U. Ude, “Overview of thin film deposition techniques,” *AIMS Materials Science*, vol. 6, no. 2. AIMS Press, pp. 174–199, 2019. doi: 10.3934/MATERSCI.2019.2.174.

[30] S. I. Shah, G. H. Jaffari, E. Yassitepe, and B. Ali, “Evaporation: Processes, Bulk Microstructures, and Mechanical Properties,” in *Handbook of Deposition Technologies for Films and Coatings*, William Andrew Publishing, 2010, pp. 135–252. doi: 10.1016/B978-0-8155-2031-3.00004-1.

[31] V. Teixeira, H. N. Cui, L. J. Meng, E. Fortunato, and R. Martins, “Amorphous ITO thin films prepared by DC sputtering for electrochromic applications,” *Thin Solid Films*, vol. 420–421, pp. 70–75, Dec. 2002, doi: 10.1016/S0040-6090(02)00656-9.

[32] P. D. Davidse and L. I. Maissel, “Dielectric thin films through RF sputtering,” *Journal of Applied Physics*, vol. 37, no. 2, pp. 574–579, 1966, doi: 10.1063/1.1708218.

[33] “Structure – composition variation in rf- sputtered films of Ge caused by process parameter changes,” vol. 1060, no. 1976, 1998.

[34] P. J. Kelly and R. D. Arnell, “Magnetron sputtering: A review of recent developments and applications,” *Vacuum*, vol. 56, no. 3, pp. 159–172, 2000, doi: 10.1016/S0042-207X(99)00189-X.

[35] J. A. Dobrowolski, J. R. Pekelsky, R. Pelletier, M. Ranger, B. T. Sullivan, and A. J. Waldorf, “Practical magnetron sputtering system for the deposition of optical multilayer coatings,” *Applied Optics*, vol. 31, no. 19, p. 3784, Jul. 1992, doi: 10.1364/ao.31.003784.

[36] A. Bashir, T. I. Awan, A. Tehseen, M. B. Tahir, and M. Ijaz, “Interfaces and surfaces,” *Chemistry of Nanomaterials*, pp. 51–87, Jan. 2020, doi: 10.1016/B978-0-12-818908-5.00003-2.

[37] J. X. J. Zhang and K. Hoshino, “Fundamentals of nano/microfabrication and scale effect,” *Molecular Sensors and Nanodevices*, pp. 43–111, Jan. 2019, doi: 10.1016/B978-0-12-814862-4.00002-8.

[38] H. G. Tompkins and J. N. Hilfiker, *Spectroscopic Ellipsometry: Practical Application to Thin Film Characterization*, 1st ed. Momentum Press, 2016.

[39] “Polarized Light - J.A. Woollam.” https://www.jawoollam.com/resources/ellipsometry-tutorial/polarized-light (accessed Jun. 10, 2022).

[40] Inc. J. A. Woollam Co., “CompleteEASE™ Data Analysis Manual.” 2011.

[41] “Thin Film Thickness - J.A. Woollam.” https://www.jawoollam.com/resources/ellipsometry-tutorial/thin-film-thickness (accessed Jun. 11, 2022).

[42] D. Salazar, R. Soto-Molina, E. G. Lizarraga-Medina, M. A. Felix, N. Radnev, and H. Márquez, “Ellipsometric Study of SiOx Thin Films by Thermal Evaporation,” *Open Journal of Inorganic Chemistry*, vol. 06, no. 03, pp. 175–182, 2016, doi: 10.4236/ojic.2016.63013.

[43] F. Urbach, “The Long-Wavelength Edge of Photographic Sensitivity and of the Electronic Absorption of Solids,” *Physical Review*, vol. 92, no. 5, p. 1324, Dec. 1953, doi: 10.1103/PhysRev.92.1324.

[44] H. Fujiwara and R. W. Collins, *Spectroscopic Ellipsometry for Photovoltaics*, vol. 2. Cham: Springer International Publishing, 2018. doi: https://doi.org/10.1007/978-3-319-75377-5.

[45] T. Lohner *et al.*, “Determination of the Complex Dielectric Function of Ion-Implanted Amorphous Germanium by Spectroscopic Ellipsometry,” *Coatings 2020, Vol. 10, Page 480*, vol. 10, no. 5, p. 480, May 2020, doi: 10.3390/COATINGS10050480.

[46] M. Di *et al.*, “Comparison of methods to determine bandgaps of ultrathin HfO 2 films using spectroscopic ellipsometry,” *Journal of Vacuum Science & Technology A: Vacuum, Surfaces, and Films*, vol. 29, no. 4, p. 041001, Jun. 2011, doi: 10.1116/1.3597838.

[47] J. van den Broek, S. Abegg, S. E. Pratsinis, and A. T. Güntner, “Highly selective detection of methanol over ethanol by a handheld gas sensor,” *Nature Communications*, vol. 10, no. 1, pp. 1–8, 2019, doi: 10.1038/s41467-019-12223-4.

[48] S. Abegg, L. Magro, J. van den Broek, S. E. Pratsinis, and A. T. Güntner, “A pocket-sized device enables detection of methanol adulteration in alcoholic beverages,” *Nature Food*, vol. 1, no. 6, pp. 351–354, 2020, doi: 10.1038/s43016-020-0095-9.

[49] G. Wen, Z. Li, and M. M. F. Choi, “Detection of ethanol in food: A new biosensor based on bacteria,” *Journal of Food Engineering*, vol. 118, no. 1, pp. 56–61, 2013, doi: 10.1016/j.jfoodeng.2013.01.006.

[50] D. Belsito *et al.*, “A toxicological and dermatological assessment of aryl alkyl alcohols when used as fragrance ingredients,” *Food and Chemical Toxicology*, vol. 50, no. SUPPL. 2, pp. S52–S99, 2012, doi: 10.1016/j.fct.2011.10.042.

[51] D. Osorio, J. Ricardo Pérez-Correa, E. Agosin, and M. Cabrera, “Soft-sensor for on-line estimation of ethanol concentrations in wine stills,” *Journal of Food Engineering*, vol. 87, no. 4, pp. 571–577, 2008, doi: 10.1016/j.jfoodeng.2008.01.011.

[52] M. Castellari, E. Sartini, U. Spinabelli, C. Riponi, and S. Galassi, “Determination of carboxylic acids, carbohydrates, glycerol, ethanol, and 5-HMF in beer by high-performance liquid chromatography and UV-refractive index double detection,” *Journal of Chromatographic Science*, vol. 39, no. 6, pp. 235–238, 2001, doi: 10.1093/chromsci/39.6.235.

[53] A. Schliesser, N. Picqué, and T. W. Hänsch, “Mid-infrared frequency combs,” *Nature Photonics*, vol. 6, no. 7, pp. 440–449, 2012, doi: 10.1038/nphoton.2012.142.

[54] D. Popa and F. Udrea, “Towards integrated mid-infrared gas sensors,” *Sensors (Switzerland)*, vol. 19, no. 9, pp. 1–15, 2019, doi: 10.3390/s19092076.

[55] P. Barritault *et al.*, “Low power CO2 NDIR sensing using a micro-bolometer detector and a micro-hotplate IR-source,” *Sensors and Actuators, B: Chemical*, vol. 182, pp. 565–570, 2013, doi: 10.1016/j.snb.2013.03.048.

[56] Q. Tan *et al.*, “Three-gas detection system with IR optical sensor based on NDIR technology,” *Optics and Lasers in Engineering*, vol. 74, pp. 103–108, 2015, doi: 10.1016/j.optlaseng.2015.05.007.

[57] T. A. Vincent and J. W. Gardner, “A low cost MEMS based NDIR system for the monitoring of carbon dioxide in breath analysis at ppm levels,” *Sensors and Actuators, B: Chemical*, vol. 236, pp. 954–964, 2016, doi: 10.1016/j.snb.2016.04.016.

[58] M. Metsälä, “Optical techniques for breath analysis: from single to multi-species detection,” *Journal of Breath Research*, vol. 12, no. 2, 2018, doi: 10.1088/1752-7163/aa8a31.

[59] U. Willer, M. Saraji, A. Khorsandi, P. Geiser, and W. Schade, “Near- and mid-infrared laser monitoring of industrial processes, environment and security applications,” *Optics and Lasers in Engineering*, vol. 44, no. 7, pp. 699–710, 2006, doi: https://doi.org/10.1016/j.optlaseng.2005.04.015.

[60] A. Sklorz, S. Janßen, and W. Lang, “Detection limit improvement for NDIR ethylene gas detectors using passive approaches,” *Sensors and Actuators, B: Chemical*, vol. 175, pp. 246–254, 2012, doi: 10.1016/j.snb.2012.09.085.

[61] K. P. Yoo *et al.*, "Fabrication, characterization and application of a microelectromechanical system (MEMS) thermopile for non-dispersive infrared gas sensors," *Measurement Science and Technology*, vol. 22, no. 11, 2011, doi: 10.1088/0957-0233/22/11/115206.

[62] H. A. Macleod, "Turning value monitoring of narrow-band all-dielectric thin-film optical filters," *Optica Acta*, vol. 19, no. 1, pp. 1–28, 1972, doi: 10.1080/713818494.

[63] C. D. Appleget, A. M. Hodge, A. M. Hodge, and C. D. Appleget, "Optical and Mechanical Characterization of Sputtered AlN/Ag Multilayer Films," *Adv. Eng. Mater*, vol. 21, p. 1801268, 2019, doi: 10.1002/adem.201801268.

[64] H. Mao *et al.*, "Ge/ZnS-Based Micromachined Fabry-Perot Filters for Optical MEMS in the Longwave Infrared," *Journal of Microelectromechanical Systems*, vol. 24, no. 6, pp. 2109–2116, Dec. 2015, doi: 10.1109/JMEMS.2015.2474858.

[65] M. Duris, D. Deubel, L. Bodiou, C. Vaudry, J. C. Keromnes, and J. Charrier, "Fabrication of Ge-ZnS multilayered optical filters for mid-infrared applications," *Thin Solid Films*, vol. 719, no. April 2020, p. 138488, 2021, doi: 10.1016/j.tsf.2020.138488.

[66] P. Wang *et al.*, "Optimised performance of non-dispersive infrared gas sensors using multilayer thin film bandpass filters," *Coatings*, vol. 8, no. 12, 2018, doi: 10.3390/COATINGS8120472.

[67] G. Pérez *et al.*, "Optical and structural characterisation of single and multilayer germanium/silicon monoxide systems," *Thin Solid Films*, vol. 485, no. 1–2, pp. 274–283, 2005, doi: 10.1016/j.tsf.2005.03.054.

[68] A. Yenisoy, C. Yesilyaprak, K. Ruzgar, and S. Tuzemen, "Ultra-broad band antireflection coating at mid wave infrared for high efficient germanium optics," *Optical Materials Express*, vol. 9, no. 7, p. 3123, 2019, doi: 10.1364/ome.9.003123.

[69] X. Tian, S. Xiong, and K. Zhang, "Improvement and coordination of spectral and mechanical properties of bandpass filter on silicon substrate for the infrared range," *Optical Engineering*, vol. 59, no. 5, 2020, doi: 10.1117/1.OE.59.5.055106.

[70] E. G. Camargo, S. Tokuo, H. Goto, and N. Kuze, "Nondispersive infrared gas sensor using InSb-based photovoltaic-type infrared sensor," *Sensors and Materials*, vol. 26, no. 4, pp. 253–262, 2014.

[71] L. Fleming, D. Gibson, S. Song, C. Li, and S. Reid, "Reducing N2O induced cross-talk in a NDIR CO2 gas sensor for breath analysis using multilayer thin film optical interference coatings," *Surface and Coatings Technology*, vol. 336, no. August 2017, pp. 9–16, 2018, doi: 10.1016/j.surfcoat.2017.09.033.

[72] C.-C. Chan, M.-C. Kao, and Y.-C. Chen, "Effects of Membrane Thickness on the Pyroelectric Properties of LiTaO3Thin Film IR Detectors," *Japanese Journal of Applied Physics*, vol. 44, no. 2, pp. 951–955, 2005, doi: 10.1143/jjap.44.951.

[73] P. Guggilla, A. K. Batra, J. R. Currie, M. D. Aggarwal, M. A. Alim, and R. B. Lal, "Pyroelectric ceramics for infrared detection applications," *Materials Letters*, vol. 60, no. 16, pp. 1937–1942, 2006, doi: 10.1016/j.matlet.2005.05.086.

[74] D. K. T. Ng *et al.*, "NDIR CO2 gas sensing using CMOS compatible MEMS ScAlN-based pyroelectric detector," *Sensors and Actuators B: Chemical*, vol. 346, no. July, p. 130437, 2021, doi: 10.1016/j.snb.2021.130437.

[75] J. H. Goldsmith, S. Vangala, J. R. Hendrickson, J. W. Cleary, and J. H. Vella, "Long-wave infrared selective pyroelectric detector using plasmonic near-perfect absorbers and highly oriented aluminum nitride," *Journal of the Optical Society of America B*, vol. 34, no. 9, p. 1965, 2017, doi: 10.1364/josab.34.001965.

[76] E. H. Putley, "The Pyroelectric Detector," *Semiconductors and Semimetals*, vol. 5, no. C, pp. 259–285, 1970, doi: 10.1016/S0080-8784(08)62817-3.

[77] E. H. Putley, "The applications of pyroelectric devices," *Ferroelectrics*, vol. 33, pp. 207–216, 1981, doi: 10.1080/00150198108008087.

[78] D. Zhang, H. Wu, C. R. Bowen, and Y. Yang, "Recent Advances in Pyroelectric Materials and Applications," *Small*, vol. 17, no. 51, pp. 1–23, 2021, doi: 10.1002/smll.202103960.

[79] A. Bruner, D. Eger, M. B. Oron, P. Blau, M. Katz, and S. Ruschin, "Temperature-dependent Sellmeier equation for the refractive index of stoichiometric lithium tantalate," *Optics Letters*, vol. 28, no. 3, p. 194, Feb. 2003, doi: 10.1364/OL.28.000194.

[80] Y. N. Wijayanto, D. Mahmudin, and P. Daud, "Design of Rectangular Optical Waveguide on LiTaO3 Crystal Using Thermal Annealled Proton Exchange Methods," *Jurnal Elektronika dan Telekomunikasi*, vol. 14, no. 1, p. 20, Jun. 2016, doi: 10.14203/JET.V14.20-23.

[81] T. Lohner *et al.*, "Determination of the Complex Dielectric Function of Ion-Implanted Amorphous Germanium by Spectroscopic Ellipsometry," *Coatings*, vol. 10, no. 5, p. 480, May 2020, doi: 10.3390/COATINGS10050480.

[82] J. A. Woollam Co, *CompleteEase Software Manual, Version 4.63*. 2011.

[83] S. Larouche and L. Martinu, "OpenFilters: Open-source software for the design, optimization, and synthesis of optical filters," *Applied Optics*, vol. 47, no. 13, pp. 219–230, 2008, doi: 10.1364/AO.47.00C219.

[84] A. Aldiyarov, M. Aryutkina, A. Drobyshev, M. Kaikanov, and V. Kurnosov, "Investigation of dynamic glass transitions and structural transformations in cryovacuum condensates of ethanol," *Low Temperature Physics*, vol. 35, no. 4, pp. 251–255, 2009, doi: 10.1063/1.3114588.

[85] Z. Liang *et al.*, "High responsivity of pyroelectric infrared detector based on ultra-thin (10 μm) LiTaO3," *Journal of Materials Science: Materials in Electronics*, vol. 26, no. 7, pp. 5400–5404, 2015, doi: 10.1007/s10854-015-3088-y.

[86] S. Nakano, Y. Kishi, T. Yokoo, K. Shibata, and Y. Kuwano, “A new-structure LiTaO3 pyroelectric infrared detector,” *Japanese Journal of Applied Physics*, vol. 20, pp. 155–158, 1981, doi: 10.7567/JJAPS.20S4.155.

[87] X. Tan *et al.*, “Non-dispersive infrared multi-gas sensing via nanoantenna integrated narrowband detectors,” *Nature Communications*, vol. 11, no. 1, pp. 1–9, 2020, doi: 10.1038/s41467-020-19085-1.

[88] S. B. Lang, “Pyroelectricity: From ancient curiosity to modern imaging tool,” *Physics Today*, vol. 58, no. 8, pp. 31–36, 2005, doi: 10.1063/1.2062916.

[89] K. D. O’Hare and P. L. Spedding, “Evaporation of a binary liquid mixture,” *The Chemical Engineering Journal*, vol. 48, pp. 1–9, 1992.

[90] P. L. Spedding, J. Grimshaw, and K. D. O’Hare, “Abnormal Evaporation Rate of Ethanol from Low Concentration Aqueous Solutions,” *Langmuir*, vol. 9, no. 5, pp. 1408–1413, 1993.

[91] C. Liu, E. Bonaccurso, and H.-J. Butt, “Evaporation of sessile water / ethanol drops in a controlled environment,” *Physical Chemistry Chemical Physics*, vol. 10, pp. 7150–7157, 2008, doi: 10.1039/b808258h.

[92] IEA, “The Future of Cooling,” 2018.

[93] EC, “Energy consumption and use by households, https://ec.europa.eu/eurostat/web/products-eurostat-news/-/ddn-20200626-1 , accessed: April, 2022.” https://ec.europa.eu/eurostat/web/products-eurostat-news/-/ddn-20200626-1 (Accessed on: 2022-04-02) (accessed Apr. 02, 2022).

[94] R. Baetens, B. P. Jelle, and A. Gustavsen, “Properties, requirements and possibilities of smart windows for dynamic daylight and solar energy control in buildings: A state-of-the-art review,” *Solar Energy Materials and Solar Cells*, vol. 94, no. 2, pp. 87–105, 2010, doi: 10.1016/j.solmat.2009.08.021.

[95] C. M. Lampert, “Chromogenic Switchable Glazing : Towards the Development of the Smart Window,” in *Proceedings of Window Innovations*, 1995, vol. 16, no. June 1995.

[96] G. Cai, P. Darmawan, X. Cheng, and P. S. Lee, “Inkjet Printed Large Area Multifunctional Smart Windows,” *Advanced Energy Materials*, vol. 7, no. 14, p. 1602598, 2017, doi: 10.1002/aenm.201602598.

[97] L. Wang, Y. Liu, X. Zhan, D. Luo, and X. Sun, “Photochromic transparent wood for photo-switchable smart window applications,” *Journal of Materials Chemistry C*, vol. 7, no. 28, pp. 8649–8654, 2019, doi: 10.1039/c9tc02076d.

[98] R. Tällberg, B. P. Jelle, R. Loonen, T. Gao, and M. Hamdy, “Comparison of the energy saving potential of adaptive and controllable smart windows: A state-of-the-art review and simulation studies of thermochromic, photochromic and electrochromic technologies,” *Solar Energy Materials and Solar Cells*, vol. 200, no. June, p. 109828, 2019, doi: 10.1016/j.solmat.2019.02.041.

[99] X. H. Li, C. Liu, S. P. Feng, and N. X. Fang, “Broadband Light Management with Thermochromic Hydrogel Microparticles for Smart Windows,” *Joule*, vol. 3, no. 1, pp. 290–302, Jan. 2019, doi: 10.1016/J.JOULE.2018.10.019/ATTACHMENT/1363E85D-8297-4AAC-A574-42A3D319C605/MMC1.PDF.

[100] Y. Zhou *et al.*, “Liquid Thermo-Responsive Smart Window Derived from Hydrogel,” *Joule*, vol. 4, no. 11, pp. 2458–2474, Nov. 2020, doi: 10.1016/J.JOULE.2020.09.001.

[101] Y. Zhou *et al.*, “Hydrogel smart windows,” *Journal of Materials Chemistry A*, vol. 8, no. 20, pp. 10007–10025, 2020, doi: 10.1039/d0ta00849d.

[102] Y. Ke, C. Zhou, Y. Zhou, S. Wang, S. H. Chan, and Y. Long, “Emerging Thermal-Responsive Materials and Integrated Techniques Targeting the Energy-Efficient Smart Window Application,” *Advanced Functional Materials*, vol. 28, no. 22, May 2018, doi: 10.1002/ADFM.201800113.

[103] J. Zhou *et al.*, “VO2 thermochromic smart window for energy savings and generation,” *Scientific Reports 2013 3:1*, vol. 3, no. 1, pp. 1–5, Oct. 2013, doi: 10.1038/srep03029.

[104] L. Kang, Y. Gao, H. Luo, Z. Chen, J. Du, and Z. Zhang, “Nanoporous thermochromic VO2 films with low optical constants, enhanced luminous transmittance and thermochromic properties,” *ACS Applied Materials and Interfaces*, vol. 3, no. 2, pp. 135–138, 2011, doi: 10.1021/am1011172.

[105] M. J. Serpe, “Gel sandwich smartens up windows,” *Nature News & Views*, vol. 565, pp. 438–439, 2019.

[106] D. Cao, C. Xu, W. Lu, C. Qin, and S. Cheng, “Sunlight-Driven Photo-Thermochromic Smart Windows,” *Solar RRL*, vol. 2, no. 1700219, pp. 1–8, 2018.

[107] Z. Xu, S. Wang, X. Y. Hu, J. Jiang, X. Sun, and L. Wang, “Sunlight-Induced Photo-Thermochromic Supramolecular Nanocomposite Hydrogel Film for Energy-Saving Smart Window,” *Solar RRL*, vol. 2, no. 11, p. 1800204, Nov. 2018, doi: 10.1002/SOLR.201800204.

[108] J. Tian *et al.*, “Sunlight-driven photo-thermochromic hybrid hydrogel with fast responsiveness and durability for energy efficient smart windows,” *Composites Part A: Applied Science and Manufacturing*, vol. 149, Oct. 2021, doi: 10.1016/J.COMPOSITESA.2021.106538.

[109] L. Zhang, H. Xia, F. Xia, Y. Du, Y. Wu, and Y. Gao, “Energy-Saving Smart Windows with HPC/PAA Hybrid Hydrogels as Thermochromic Materials,” *ACS Applied Energy Materials*, vol. 4, no. 9, pp. 9783–9791, Sep. 2021, doi: 10.1021/ACSAEM.1C01854/SUPPL_FILE/AE1C01854_SI_001.PDF.

[110] R. L. Sala, R. H. Gonçalves, E. R. Camargo, and E. R. Leite, “Thermosensitive poly(N-vinylcaprolactam) as a transmission light regulator in smart windows,” *Solar Energy Materials and Solar Cells*, vol. 186, no. July, pp. 266–272, 2018, doi: 10.1016/j.solmat.2018.06.037.

[111] Y. Wang *et al.*, "Smart Window Based on Temperature-Responsive Starch Hydrogel with a Dynamic Regulation Mode," *Industrial and Engineering Chemistry Research*, vol. 59, no. 48, pp. 21012–21017, Dec. 2020, doi: 10.1021/ACS.IECR.0C04029/SUPPL_FILE/IE0C04029_SI_001.DOCX.

[112] Y. S. Yang, Y. Zhou, F. B. Yin Chiang, and Y. Long, "Temperature-responsive hydroxypropylcellulose based thermochromic material and its smart window application," *RSC Advances*, vol. 6, no. 66, pp. 61449–61453, 2016, doi: 10.1039/c6ra12454b.

[113] S. Kiruthika and G. U. Kulkarni, "Energy efficient hydrogel based smart windows with low cost transparent conducting electrodes," *Solar Energy Materials and Solar Cells*, vol. 163, no. December 2016, pp. 231–236, 2017, doi: 10.1016/j.solmat.2017.01.039.

[114] T. G. La, X. Li, A. Kumar, Y. Fu, S. Yang, and H. J. Chung, "Highly Flexible, Multipixelated Thermosensitive Smart Windows Made of Tough Hydrogels," *ACS Applied Materials and Interfaces*, vol. 9, no. 38, pp. 33100–33106, 2017, doi: 10.1021/acsami.7b08907.

[115] M. Wang *et al.*, "Binary solvent colloids of thermosensitive poly(N - isopropylacrylamide) microgel for smart windows," *Industrial and Engineering Chemistry Research*, vol. 53, no. 48, pp. 18462–18472, 2014, doi: 10.1021/ie502828b.

[116] M. Wang *et al.*, "Electrochromic Smart Windows Can Achieve an Absolute Private State through Thermochromically Engineered Electrolyte," *Advanced Energy Materials*, vol. 9, no. 21, p. 1900433, 2019, doi: 10.1002/aenm.201900433.

[117] G. Xu *et al.*, "Thermochromic Hydrogels with Dynamic Solar Modulation and Regulatable Critical Response Temperature for Energy-Saving Smart Windows," *Advanced Functional Materials*, vol. 32, no. 5, p. 2109597, 2022, doi: 10.1002/adfm.202109597.

[118] H. G. Schild, "Poly(N-isopropylacrylamide): experiment, theory and application," *Progress in Polymer Science*, vol. 17, no. 2, pp. 163–249, 1992, doi: 10.1016/0079-6700(92)90023-R.

[119] M. H. Futscher, M. Philipp, P. Müller-Buschbaum, and A. Schulte, "The Role of Backbone Hydration of Poly(N-isopropyl acrylamide) Across the Volume Phase Transition Compared to its Monomer," *Scientific Reports*, vol. 7, no. 1, pp. 1–10, 2017, doi: 10.1038/s41598-017-17272-7.

[120] J. L. Lin, M. H. Wu, C. Y. Kuo, K. Da Lee, and Y. L. Shen, "Application of indium tin oxide (ITO)-based microheater chip with uniform thermal distribution for perfusion cell culture outside a cell incubator," *Biomedical Microdevices*, vol. 12, no. 3, pp. 389–398, 2010, doi: 10.1007/s10544-010-9395-4.

[121] W. S. Cheong *et al.*, "High-Performance Transparent Electrodes for Automobile Windshield Heaters Prepared by Combining Metal Grids and Oxide/Metal/Oxide

Transparent Electrodes," *Advanced Materials Technologies*, vol. 4, no. 4, p. 1800550, Apr. 2019, doi: 10.1002/ADMT.201800550.

[122] C. Ji, D. Liu, C. Zhang, and L. Jay Guo, "Ultrathin-metal-film-based transparent electrodes with relative transmittance surpassing 100%," *Nature Communications 2020 11:1*, vol. 11, no. 1, pp. 1–8, Jul. 2020, doi: 10.1038/s41467-020-17107-6.

[123] J. Jang *et al.*, "Rapid production of large-area, transparent and stretchable electrodes using metal nanofibers as wearable heaters with wireless operations," *Nature Publishing Group*, p. 432, 2017, doi: 10.1038/am.2017.172.

[124] J. Y. Lee, S. T. Connor, Y. Cui, and P. Peumans, "Solution-processed metal nanowire mesh transparent electrodes," *Nano Letters*, vol. 8, no. 2, pp. 689–692, Feb. 2008, doi: 10.1021/nl073296g.

[125] D. Sui, Y. Huang, L. Huang, J. Liang, Y. Ma, and Y. Chen, "Flexible and Transparent Electrothermal Film Heaters Based on Graphene Materials," *Small*, vol. 7, no. 22, pp. 3186–3192, Nov. 2011, doi: 10.1002/SMLL.201101305.

[126] J. Du, S. Pei, L. Ma, and H. M. Cheng, "25th anniversary article: Carbon nanotube- and graphene-based transparent conductive films for optoelectronic devices," *Advanced Materials*, vol. 26, no. 13, pp. 1958–1991, 2014, doi: 10.1002/adma.201304135.

[127] J. Yun, "Ultrathin Metal films for Transparent Electrodes of Flexible Optoelectronic Devices," *Advanced Functional Materials*, vol. 27, no. 18, p. 1606641, May 2017, doi: 10.1002/adfm.201606641.

[128] T. Gyenes, A. Szilágyi, T. Lohonyai, and M. Zrínyi, "Electrically adjustable thermotropic windows based on polymer gels," *Polymers for Advanced Technologies*, vol. 14, no. 11–12, pp. 757–762, 2003, doi: 10.1002/pat.391.

[129] A. K. Singh, S. Kiruthika, I. Mondal, and G. U. Kulkarni, "Fabrication of solar and electrically adjustable large area smart windows for indoor light and heat modulation," *Journal of Materials Chemistry C*, vol. 5, no. 24, pp. 5917–5922, 2017, doi: 10.1039/c7tc01489a.

[130] D. Lee, G. Bang, M. Byun, and D. Choi, "Highly flexible, transparent and conductive ultrathin silver film heaters for wearable electronics applications," *Thin Solid Films*, vol. 697, p. 137835, Mar. 2020, doi: 10.1016/J.TSF.2020.137835.

[131] K. D. Kim *et al.*, "Decoupling optical and electronic optimization of organic solar cells using high-performance temperature-stable TiO2/Ag/TiO2 electrodes," *APL Materials*, vol. 3, no. 10, p. 106105, 2015, doi: 10.1063/1.4933414.

[132] D. Choi, "The Transmittance Modulation of ZnO/Ag/ZnO Flexible Transparent Electrodes Fabricated by Magnetron Sputtering," *Journal of Nanoscience and Nanotechnology*, vol. 20, no. 1, pp. 379–383, Aug. 2020, doi: 10.1166/jnn.2020.17238.

[133] T. Chang, X. Cao, Y. Long, H. Luo, and P. Jin, "How to properly evaluate and compare the thermochromic performance of VO 2 -based smart coatings," *Journal*

of Materials Chemistry A, vol. 7, no. 42, pp. 24164–24172, Oct. 2019, doi: 10.1039/C9TA06681K.

[134] T. Munk *et al.*, "Investigation of the phase separation of PNIPAM using infrared spectroscopy together with multivariate data analysis," *Polymer (Guildf)*, vol. 54, no. 26, pp. 6947–6953, 2013, doi: 10.1016/j.polymer.2013.10.033.

[135] Y. Shi, C. Ma, L. Peng, and G. Yu, "Conductive 'smart' hybrid hydrogels with PNIPAM and nanostructured conductive polymers," *Advanced Functional Materials*, vol. 25, no. 8, pp. 1219–1225, Feb. 2015, doi: 10.1002/ADFM.201404247.

[136] S. Y. Lin, K. S. Chen, and R. C. Liang, "Thermal micro ATR/FT-IR spectroscopic system for quantitative study of the molecular structure of poly(N-isopropylacrylamide) in water," *Polymer (Guildf)*, vol. 40, no. 10, pp. 2619–2624, 1999, doi: 10.1016/S0032-3861(98)00512-6.

[137] B. Sun, Y. Lin, and P. Wu, "Structure analysis of poly(N-isopropylacrylamide) using near-infrared spectroscopy and generalized two-dimensional correlation infrared spectroscopy," *Applied Spectroscopy*, vol. 61, no. 7, pp. 765–771, 2007, doi: 10.1366/000370207781393271.

[138] J. H. Park *et al.*, "Preparation and Properties of Thermoresponsive P(N-Isopropylacrylamide-co-butylacrylate) Hydrogel Materials for Smart Windows," *International Journal of Polymer Science*, vol. 2019, 2019, doi: 10.1155/2019/3824207.

[139] R. Yoshida *et al.*, "Comb-type grafted hydrogels with rapid deswelling response to temperature changes," *Nature*, vol. 374, no. 6519, pp. 240–242, 1995, doi: 10.1038/374240a0.

[140] V. M. Chauhan *et al.*, "Thermo-optical characterization of fluorescent rhodamine B based temperature-sensitive nanosensors using a CMOS MEMS micro-hotplate," *Sensors and Actuators. B, Chemical*, vol. 192, p. 126, 2014, doi: 10.1016/J.SNB.2013.10.042.

[141] D. Lee and D. Choi, "Highly thermostable ultrathin planar Ag transparent heaters," *Microelectronic Engineering*, vol. 251, no. July 2021, 2022, doi: 10.1016/j.mee.2021.111658.

[142] "ASTM G173-03 Standard Tables of Reference Solar Spectral Irradiances: Direct Normal and Hemispherical on a 37° Tilted Surface, Annual Book of ASTM Standards, American Society for Testing and Materials."